Università degli studi di Padova

Dipartimento di Scienze Chimiche

Corso di laurea Magistrale in Chimica

Computational investigation of defects in transition metal dichalcogenides for quantum computing

Relatore: Prof. Stefano Corni

Controrelatore: Prof. Daniel Forrer

Candidato: Alessandro Bello

Matricola: 1210399

Anno Accademico 2022/2023

II

Abstract

Quantum computing is a very active interdisciplinary area of research, arose in the first few years of the 80s. The quantum computers that we can use today are the results of the effort from the various fields involved such as Computer Science, Engineer, Mathematics, Physics and Chemistry. When we compare a quantum computer and a classical one on certain task it has been proven that the former speed-up exponentially the calculation by reducing the time needed to perform it. The role of chemistry in quantum computing is dual, on one side researchers are trying to find the analogue of the transistor for a quantum computers. To reach this goal there is the need to test different materials to find which one presents the most suitable characteristics that make it scalable, manipulable and can be miniaturized. On the other hand chemists want to use the exponential boost of quantum computers to run simulation of chemical interest, and this in turn may lead to discovery of new drugs and new materials. Thus, in some ways chemistry is at the root and at the leaves of the quantum computing tree.

The focus of this thesis will be the development of a low computational cost calculation protocols that can be used to screen many different materials at once. This is done in order to simulate, at the level of ab initio theories, interesting properties of quantum materials (useful for building quantum computers). In the literature the screening is often not taken into consideration and most of the calculation are based on a singular material at a very expensive computational cost. Instead, we will use the main ideas behind Density Functional Theory (DFT) because we envision that it can lead to a simple way of determining the most suitable material. Moreover we will discuss the theory of ΔSCF method, how can be useful in our case and what are its limitations.

To evaluate the quality of our protocols we will consider materials like transition metals dichalcogenides (TMDs) found in literature and compare our simulation results reference simulations from the recent literature. We took in consideration WS_2 and MoS_2 with and without a carbon defect in them. TMDs have attracted the researchers attention for over a decade, because they exhibit a plethora of different properties and the potential for being used in various fields including electronic, optoelectronic, sensing and energy storage. Moreover these are an ideal 2D host for quantum defects. These defects can be engineered on demand at atomic size level precision, which holds a promise for a scalable and addressable Quantum Processing Unit (QPU).

As a perspective of this research we envision that this protocol can be useful to screen not only

different materials, but dozens of combinations of different defects, transition metals and number of defects in the system. This is paramount to scan the many possible good materials with the right parameters needed. Then, after this screening we will select the most promising ones with a higher level of theory to corroborate our results and galvanize the attention of experimentalists to synthesize such materials.

Contents

Introduction

Quantum computing is a multidisciplinary field comprising aspects of computer science, physics, and mathematics that utilizes quantum mechanics to solve complex problems on a time scale shorter than on classical computers. One field can benefit enormously from this kind of machines, chemistry. In fact one of the most promising suggested applications of quantum computing is solving classically demanding chemistry problems[1]. This may help to answer unresolved questions about phenomena such as high temperature superconductivity, solid-state physics, transition metal catalysis, and certain biochemical reactions[1]. This increased understanding may help us to refine, and perhaps even one day design, new compounds of scientific and industrial importance[1]. But there are hindrances along this road. First of all we have to find a proper platform on which to run such simulations, and then find a quantum algorithm that is quantitatively faster (in terms of time of calculation) than the classical analogue.

There is a common misconception that quantum computers are just better than classical computer in every domain. But quantum computers are in fact really specialized machines that can run only certain tasks faster than the classical counterpart. In order to exploit some computational power, there is thus the need to build more stable and reliable qubit and this is something that the community have to tackle in some ways.

The major platforms currently being explored for quantum computing are semiconductor quantum dots (QDs)[2], spin defects in wide-bandgap materials[3], superconducting qubits[4], topologically protected solid-state systems[5], Rydberg atoms[6], ion trap systems[7], and photonic quantum computing [8][9]. As we can see there are many different approaches to solve the problem of a good qubit and thus the need for new materials is surging because the technologies available now either do not scale well or they scale but with detrimental effect on the stability of the qubit, leading to an amount of non-predictable errors that can make the results from the calculation unusable. Here we will introduce some of the current proposals of quantum materials potentially useful for building qubit and analyse the properties of each one. Then we will focus on a specific material to be compared with our calculation.

1.1   Introduction to qubits

A quantum computer (QC) exploit the laws of quantum physics using qubits as its unit of compu-
tation, leading to possibly exponential speed-up in known algorithm and simulations of physical
systems. Qubits are described as mathematical objects with some specific properties. Just as a clas-
sical bit has a state, either 0 or 1, a qubit also has a state. Two possible eigenstates for a qubit are
$|0\rangle$ and $|1\rangle$. What they differs is in the number of possible states to which they get access, since we
can form a linear combination of states with the qubits of the type:

$$|\psi\rangle = \alpha |0\rangle + \beta |1\rangle \tag{1.1}$$

where in general α and β are complex numbers. Said in another way a qubit is a vector in a two
dimensional complex vector space. The special states $|0\rangle$ and $|1\rangle$ are known as computational basis
states, and form an orthonormal basis for this vector space.

Classical computers usually determine the state of a transistor with either 0 or 1 and retrieve these
values from the memory all the time. Instead by the laws of quantum mechanics we can acquire only
much more restricted information about a quantum state, since we will not get as an output 100% of
the time only 0 or only 1 because these depends on the amplitude of the wavefunctions describing
them. In fact we have to run our calculation many many times and collect a statistics of the states.
Thus when we measure a qubit we get either 0 with probability $|\alpha|^2$ or 1 with probability $|\beta|^2$. With
the constrain that $|\alpha|^2 + |\beta|^2 = 1$. Geometrically this tells us that a qubit has to be normalized to 1
and thus in general a qubit's state is a unit vector in a two-dimensional complex vector space.

The superposition ability of the qubits have no analogous with the common sense understanding
of the physical world around us. If a classical bit can be described as a fair coin showing either head
or tail, the same cannot be said for the qubits. A qubit state can in fact have access to a continuum
of states between $|0\rangle$ and $|1\rangle$ until the system is observed. Upon measurement only the "0" or the
"1" state can result. For example in the state:

$$|\psi\rangle = \frac{1}{\sqrt{2}} |0\rangle + \frac{1}{\sqrt{2}} |1\rangle \tag{1.2}$$

the probability of having as a result "0" is exactly fifty percent or $|1/\sqrt{2}|^2$ and the same can be
said for "1".

One geometrical idea that can be useful to depict a qubit is the following. Since $|\alpha|^2 + |\beta|^2 = 1$
we may rewrite the Equation 1.2 as:

$$|\psi\rangle = \cos\frac{\theta}{2} |0\rangle + e^{i\varphi} \sin\frac{\theta}{2} |1\rangle . \tag{1.3}$$

where θ and φ are real numbers. The numbers θ and φ define a point in a 3D sphere as in
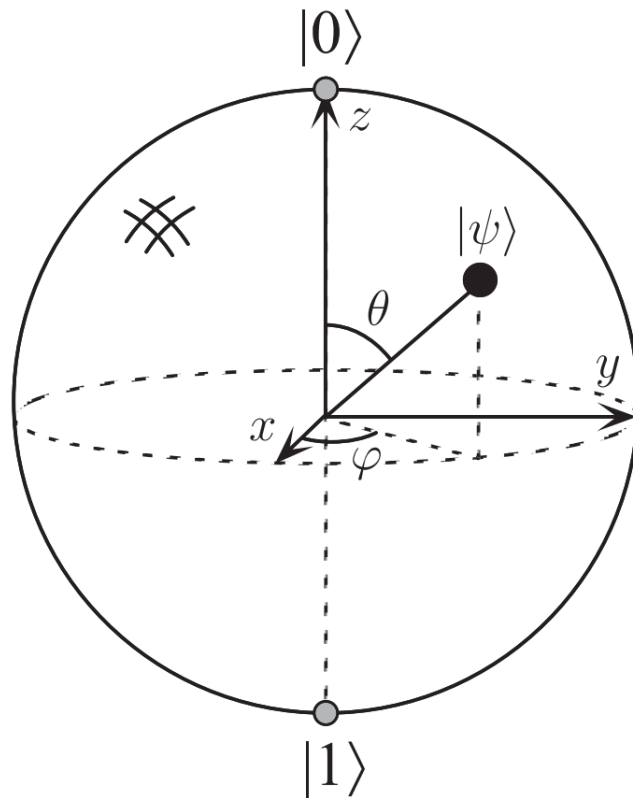
Figure 1.1: Bloch sphere representation of a qubit.

Figure 1.1. Many operations acted on a qubit can be clearly visualized with the Bloch sphere picture.

Now that we introduced the concept of qubit, where does the speed-up of a quantum computer comes from? In principle to represent a superposition of 2^n states classically the resources needed to represent such systems grows exponentially with the number of states n. In contrast, in quantum theory, a general superposition of 2^n states can be represented in n entangled 2-level states[10]. Entangled means essentially that the properties of the qubits are correlated. Thus the amount of physical resources needed will grow only linearly with n. This is the main speed-up that we can expect from a quantum computer.

1.2 Minimum set of requirements to build a Quantum Computer

With the advent of new technologies we need a template to follow in order to build a system that conforms to the architecture of a quantum computer. The criteria one should follow were developed by DiVincenzo[11] in 2000 and are the followings:

(i) There exist a scalable physical system with well characterized qubits.

(ii) The qubits can be initialized to a known state.

(iii) The decoherence time of the qubits is longer than the time it takes to perform a quantum gate operation on it.

(iv) A set of universal quantum gates exist for the qubit(s).

(v) The qubit should be amenable to be measured.

Let us explain some of the criteria shown above. The first one clearly states that we need physical system where the qubits can manifest their peculiar properties. A qubit is said to be "well characterized" when several conditions are met. Its physical parameters should be known, including the Hamiltonian from which one can choose the eigenstates as $|0\rangle$ and $|1\rangle$. Said in another way, we should know what is representing the $|0\rangle$ and $|1\rangle$ in a quantum mechanical picture, e.g. knowing the possible wave functions of the ground state of the system and the first excited state respectively. The presence of coupling to other states and external fields should be also known. If, for example a chosen qubit has three, four, etc. levels that can be excited, the probability of the system going into these states should be small in order to stay on the computational basis chosen as $|0\rangle$ and $|1\rangle$. How small will be determined by the capabilities of quantum error correction. Quantum Error Correction (QEC) is a procedure used in quantum computing to protect quantum information from errors due to quantum noise. QEC is theorised as essential to achieve fault tolerant quantum computing that can reduce the effects of noise on stored quantum information, faulty quantum gates, faulty quantum preparation, and faulty measurements[12].

The second criteria arises from computing requirements that registers (a system comprising many manipulable qubits) should be initialized to a known value before the start of the computation. There's also another requirement for the initialization: QEC. This in fact requires a continuous fresh supply of qubits in a stable state (like a $|0\rangle$ quantum state) because we need a reliable source of qubits that can be addressed without the coupling with the environment. The need for a continuous supply can be challenging and since QEC is still quite some time ahead, this problem can be postponed later. Theoretically the initialization step has to be faster than the time for the operation to be applied to a qubit. A practical approach implies that the qubit has to be reinitialized away from the region in which active computation is taking place and brought back after the initialization has finished, but this is rather unfavorable and we would prefer a fast initialization.

The third criteria states the required time for a gate (operation) to be performed has to be within the coherent time of a qubit,which is the duration of time that qubits can be manipulated during a calculation. Decoherence is fundamental to quantum physics because it's one of the principal mechanism for the emergence of classical behaviour[13]. Decoherence simply put it's the loss of quantum coherence, e.g. a qubit state that is perturbed by some other states of the environment or other qubits' states. This is detrimental if it acts for a very long time and can potentially destroy the capabilities of the quantum computer that becomes not so different from a classical one. The most simple definition of decoherence can be the characteristic time for a generic spin system to couple with the environment or other species in it. This is what mainly scientists are focused on because it imposes a limit in the number of operation a qubit can do [14]. If we want to talk about coherence

instead this tells us how long a qubit retains its information and in turn gives us a lifetime with which we can compare different qubits.

The fourth criteria states that in order for a quantum algorithm to work it is necessary to specify a sequence of unitary transformations $U_1, U_2, U_3, \ldots$ that acts on a small number of qubits. Unitary transformations are those who satisfies the following relation $U^{-1} = U^\dagger$ and says that the inverse of the transformation is equal to its conjugate transpose, if we represent the transformation as a matrix. The way in which we encode the physical information is to identify Hamiltonians that reflects these unitary transformations, e.g. $U_1 = e^{iH_1 t/\hbar}$ then each apparatus should be designed so that H_1 can be turned on from 0 to t, turned off, then H_2 turned on from time t to $2t$ etc. This immediately poses a problem for quantum computing because, how are we going to represent states with three-qubit unitary transformation? One way is to decompose the operation in sequences of one or two-body interactions[15] [16]. We should include also that not only there's a problem with the implementation, but also with the classical interactions that can "sneak-in" from the apparatus itself. In fact, even the apparatus is a quantum system that may entangle with the single qubits. Since these effects can interfere with states of each individual qubits they have to be taken into account properly for each individual system. Some of these requirements are fundamental to error correction that requires fully parallel operation on small portion of the qubits simultaneously. This can be a real challenge for some proposal that have to use a so called "bus-qubit" to mediate the signal between each interaction [15]. On the other hand some solid-state proposals does allow for sufficient parallelism with the constraint of interactions only among nearest neighbours in a lattice.[17] But even in these type of systems there will be both systematic and random errors in the way we expect to implement a necessary Hamiltonian. We have two strategies to handle these kind of errors, careful calibration and error correction which aims to produce reliable results from unreliable gates, if the magnitude of unreliability is small enough. How much is small enough? That should be in the order of 10^{-4} to 10^{-5} errors per gate operation [15]. The great deal with QEC is, there is no precondition on having to create new type of gates. We only need the one and two-qubits that are usually built for computation.

The fifth criteria is finally the requirement that a qubit has to be read-out and this requires some ability to measure specific qubits and leave the others untouched. In an ideal measurement if a qubit's state is of the type:

$$|\psi\rangle = \sqrt{p}\,|0\rangle + \sqrt{(1-p)}\,|1\rangle \tag{1.4}$$

then the measurement should return "0" with probability p and "1" with probability $1-p$ independently of other parameters in the system. This has to be done without changing the states of other qubits in the quantum computer in order to measure selectively the qubit of interest. In the lucky case in which the measurement is a "non-destructive" one, we can have both the outcome "0" and the qubit in the state $|0\rangle$ that can be also used in second criteria (ii) above-mentioned. This is in the

ideal case of 100% quantum efficiency that can be seldom be satisfied. But we can do with much less in fact even with a quantum efficiency of 90%, we just need to rerun the calculation as many times as we want to achieve the needed reliability.[11] Even quantum efficiencies as low as 1% can be and are used for quantum computing: this is the so-called bulk model of Nuclear Magnetic Resonance (NMR), that was one of the first quantum computers to be used.[18]

Satisfying these requirements can lead to performant devices that can be used as a QPU. Let us look now at two example of real implementations of those criteria here enounced.

1.3 Examples of Quantum Computer really built

There are two major type of QCs that one usually encounters in the NISQ (Noisy Intermediate Scale Quantum computer) era, which is the stage QCs are nowadays. These are *Ion-Trap* and *Superconducting* QPU. We will omit an explanation for the Superconducting qubits because they are out of the scope of this thesis[19], but we will delve in how it works an Ion-Trap QC, in fact they provide analogies for the kind of systems investigated later in this thesis. There are many other examples[20] but these are the ones that respect the most of Di Vincenzo criteria, and they work in a similar to the device that we are going to study in detail in this thesis.

1.3.1 Ion-Trap qubits

In the trapped ion approach there are atoms (such as Yb or ^{40}Ca) that are ionized with lasers and trapped in an electric potential field to form a string of adjacent ions, this is due to the geometry of the apparatus that can confine the charged ions with an electrical field. An additional laser is then used to measure the state of the qubits prepared. In order to have a clear signal from the measure and a good manipulation of those ions the system need to be in the condition of Ultra High Vacuum (in the range of $10^{-9} - 10^{-12}$ mbar)[21]. This allows a good initialization and read-out because there is a negligible portion of interfering atoms in the ion trap chamber.

One chief advantages in trapped ions QCs is the straightforward methodology to localize ions in specific regions of a trap for long periods of time. For this purpose we need a method of confining charged ions in an effective way. Usually a time-dependent electric field or a combination of static electric and magnetic fields are required for such localization[22]. A surprising advantage comes from the measurement of the selected states. For example if we want to measure a state we also want consistent results if the measurement is repeated a number of times. Ion trapped qubit allow to read information easily in a *non-demolition* fashion, meaning we can continue with other operation because the system automatically reinitialize.

For a further comprehension on how a quantum computer really works internally we can use as example the case of ^{40}Ca$^+$ is one of the most common technologies currently studied[24]. We refer
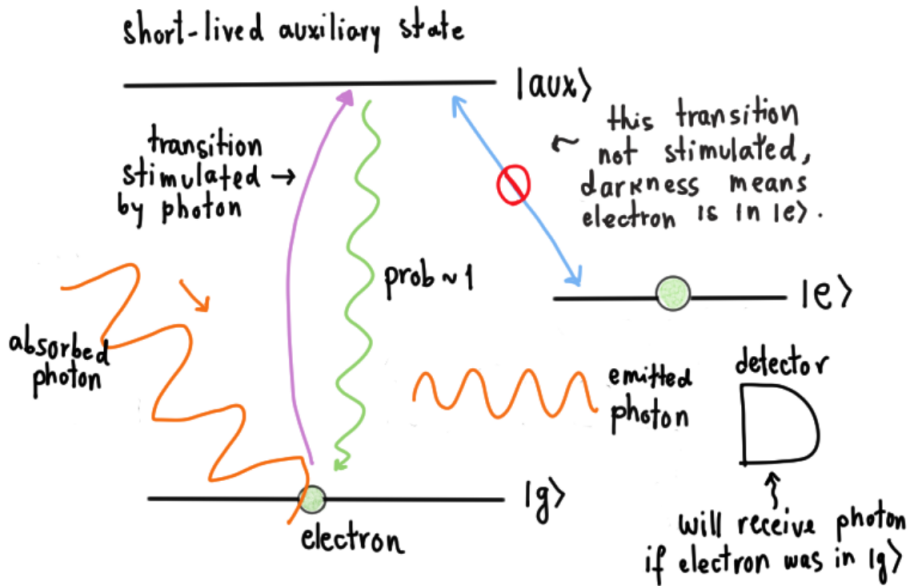
Figure 1.2: Energy level scheme in ^{40}Ca$^+$ ion. The flat lines represents the energy levels chosen as qubit. Each line represents a possible transition and the wiggly lines a possible photon emission. Moreover on the right we can see a photo-detector recording the emitted photon from the decay of the excited state $|aux\rangle$. Image take from Ref. [23]

to the states of some atoms in an ion trap using the spectroscopic notation $^{2s+1}L_j$ where $2s + 1$ is the spin multiplicity, L refers to the orbital angular momentum written as $S, P, D, F, \ldots$ for $l = 0, 1, 2, 3, \ldots$, and j is the total angular momentum quantum number. In this typical setup the energy levels of the ions used are principally $^2S_{1/2}$ as the $|0\rangle$ state, the $^2P_{1/2}$ as a bright state which can be recorded by fluorescence, and the $^2D_{1/2}$ as the $|1\rangle$ state which is dark. The transition and consequent manipulation of the states involved are controlled by laser beams in the UV range. The number of qubits may vary from tens to about fifty within the same system, although the numbers nowadays are continually evolving[25][26][24].

Now to simplify the discussion about the measurement method, further described, we will refer to $^2S_{1/2}$ as $|g\rangle$, $^2P_{1/2}$ as $|aux\rangle$ and $^2D_{1/2}$ as $|e\rangle$ in order to gain more insight in the measurement system without bothering with the spectroscopic notation.

The measurement method is similar, in principle, on that of optical pumping, in which light is used to raise electrons from a lower energy level to a higher one. Using as a prototypical example, the ^{40}Ca$^+$ ion as sketched in Figure 1.2, we have two states $|g\rangle$ and $|aux\rangle$ and we can promote one electron from the $|g\rangle$ to the $|aux\rangle$ via laser with wavelength $397\,nm$. Since the $|aux\rangle$ has a lifetime of $7\,ns$ the system returns back to the ground state emitting a photon of the same wavelength that can be collected (using a lens and a photomultiplier to transform the light in a sufficient strong enough electric signal). This tell us that the system was indeed in the state $|g\rangle$ because the transition from the other state $|e\rangle$ is dark. Conversely if we had stimulated the ion with the above-mentioned laser and recorded nothing from the fluorescence spectra we would have been sure that the system was in the state $|e\rangle$. If we call $|g\rangle = |1\rangle$ and $|e\rangle = |0\rangle$ we have our standard qubit basis[23].

It has to be noted that a similar approach can be used even in semiconductor qubits and in fact

we will see a similar electronic structure for our proposals later on in this thesis.

1.4 Quantum materials to build quantum computers: state-of-the-art

We have, very briefly, explained how an Ion Trap qubit works but here we have to stress further that we still have to discover an analogous of the transistor for quantum chip. There are valid proposals that are being implemented right now, but the two main problems that afflicts them are huge, namely, the coherence time, still too short to have any reliable calculation result, and the extreme physical conditions at which they operate. These problems will result in an hindrance to scalability and accessibility of these devices. It is therefore imperative to have high purity materials with interfaces free of defects and trap states. In solid state quantum systems, it is somewhat intuitive to consider new materials with intrinsic quantum properties themselves. Now we will review some proposals from the literature regarding new materials that could solve these problems.

1.4.1 2D Materials
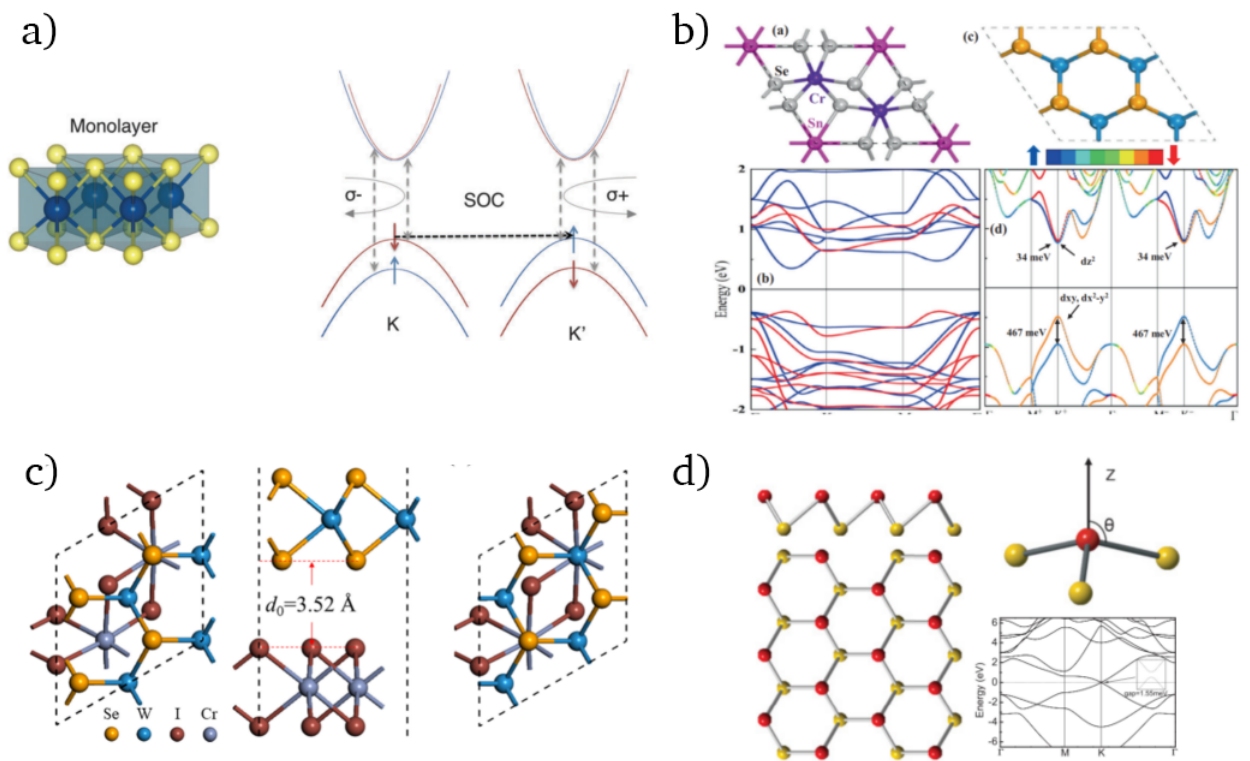
Figure 1.3: On panel a): example of MoS_2 monolayer crystal structure and band structure with valleys identified as K and K', SOC stands for Spin Orbit Coupling. On panel b): monolayers of $CrSnSe_3$ on the left and WSe_2 on the right and their respective band structures. On panel c): crystal structure of WSe_2 superposed with CrI_3. On panel d): an example of Silicene, an analogous of graphene for Si[27].

When atoms are brought together in close proximity to form a crystal, the electrons of the constituent atoms interact with each other and with the atoms themselves, giving rise to distinct bands

of energy that determine the electronic properties of the crystal-line material. Along each path of the crystal there can be a different manifold of bands that can be used for electronic properties of interest. In semiconducting crystals, electrons populate a filled band of allowed states known as the valence band. There is also an unfilled band of higher energy states known as the conduction band in which electrons can be excited by some source of energy. The gap of energy that separates these valence and conduction, maxima and minima respectively, is called band-gap. These contains no allowed states. These maxima and minima we refer to as valleys, and devices exploiting the fact that electrons, holes, or excitons are present in one valley versus another we refer to as valleytronic devices. Selectively populating one momentum-distinguishable valley versus another creating a valley polarization is the key enabling feature of valleytronics. One example that possess this kind of properties is without any doubt TMDs (Transition Metal Dichalcogenides) as in Figure 1.3 a). The valleys in these material are degenerate. Meaning that at crystal point K and K' the VBM (Valence Band Maxmima) are degenerate in energy as in the top left panel in Figure 1.3 a). To lift-off the degeneracy in the system we need to make some states more stable than others using a magnetic field, so exploiting the . This breaks the degeneracy and thus one can use some circularly polarized light to selectively address the K (using right circularly polarized light σ^-) and the K' (using left circularly polarized light σ^+) valley to create a two level system and use it as a qubit[28]. These properties are shared among different species of the same brute formula MX_2 where M is a transition metal (namely Mo, W, Re, . . .) and X is a chalcogenide (namely O, S, Se, Te, . . .), so called TMDcs. Indeed we can find a rich line of research focusing just on these materials and in combination with other substrates, such as, for example $WSe_2/CrSnSe_3$[29] as in Figure 1.3 b) or WSe_2/CrI_3[30] as in Figure 1.3 c) that allow to improve the control over the valley pseudospin degree of freedom[27]. Moreover there are quite interesting properties to be investigated in materials simalar to graphene like Silicene in Figure 1.3 d).

The problem faced with these kinds of materials are related to the single addressability of these "qubits". Making a single addressable qubit from these materials can be a real challenge. Suppose to shine laser light and excite a particle and create an exciton in this material. Then this will generate other pairs of holes-electrons throughout the material. In this way we are not respecting the second DiVincenzo Criteria, requiring that we should initialize and control a known state of the material.

1.4.2 Nanowires

Semiconducting nanowires (NWs) as in Figure 1.4 and nanotubes (NTs) have highly anisotropic electronic structures and strong spin-orbit interaction. The intrinsic lateral confinement of carriers simplifies device design, and the strong Spin Orbit Coupling (SOC) enables fast, all-electrical control since $H_{SOC} \propto (\vec{E} \times \vec{p}) \cdot \vec{\sigma}$, where $\vec{E}$ is the electric field, $\vec{p}$ the momentum, and $\vec{\sigma}$ the Pauli matrices and H_{SOC} is the eigenvalue of Hamiltonian in the SOC regime[31]. The SOC can thus create
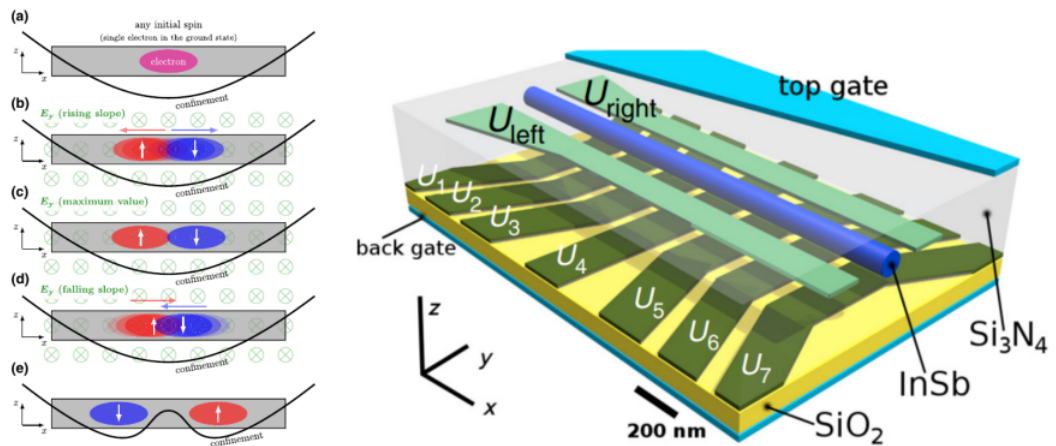
Figure 1.4: Scheme of a working NW qubit[27].

a manipulation point to read and write possible qubits in the desired configuration. InSb and InAs have attracted attention for quantum devices due to their high electron mobility[32], large Lande g-factor[33], and strong spin orbit coupling. Fast, all-electrical initialization[27] and manipulation of spin-orbit qubits make InSb and InAs NWs promising for future QD devices. In a nutshell the nanowire contains an electron that can be trapped and it's potential energy surface be modified as we like to manipulate the spin states of the electron. In this kind of setup it was possible to initialize the qubit into a known state.

1.4.3 Organic Qubits

Organic molecules have emerged as an unconventional potential qubit system[27]. Possible qubits may be realized by the spins of Molecular NanoMagnets (MNMs), photogenerated states, and radical spins. The chemical tunability of these complexes is a unique feature that allows greater room for optimization and molecular design.

A promising application of MNMs is quantum memories that are the quantum-mechanical version of ordinary computer memory. Whereas ordinary memory stores information as binary states (represented by "1"s and "0"s), quantum memory stores a quantum state for later retrieval. Unlike the classical memory of everyday computers, the states stored in quantum memory can be in a quantum superposition, giving much more practical flexibility in quantum algorithms than classical information storage. Multiple ancilla qubits can be encoded in the multilevel system and can be used to encode one logical qubit. This is crucial because as said in section 1.1 the storage of the states' amplitudes can grow exponentially with the number of qubits, thus we need some sort of quantum analogue of a RAM as shown here. Moreover, molecules can be designed to have multiple coupled
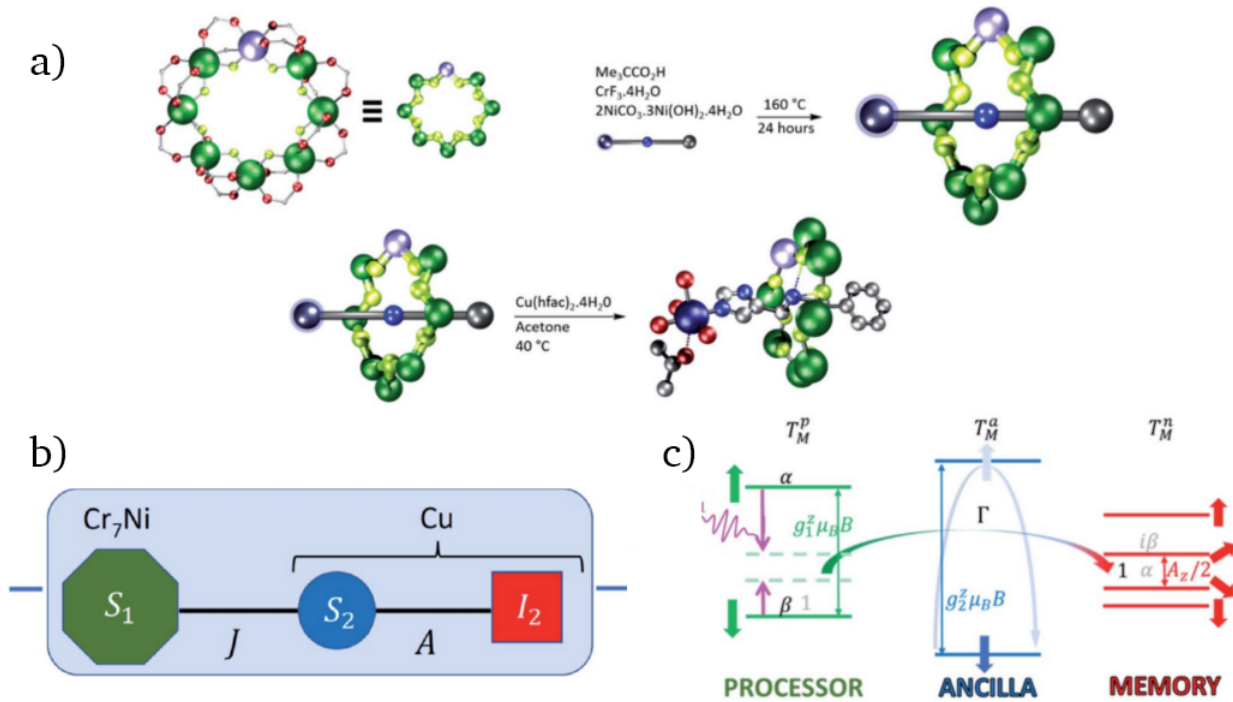
Figure 1.5: Scheme of an Organic qubits. On panel a): reaction path to synthetize the material. On panel b): a representation of the qubit processor (green), ancilla (blue), and qudit memory (red). On panel c): energy level representation of qubit processor, ancilla qubit and qudit memory.[34].

qubits or qudits (quantum-dits, a d-based system of computation in which we do not have just two states 0 and 1, but d number as basis, e.g. a qutrit is a quantum system with three states as basis of computation 0, 1 and 2), one of which serves as a memory while the rest act as a processor or ancilla bit for QEC. Ancilla qubits are some extra qubits being used to achieve some specific goals in computation whose values are known a priori. This allow an initialization of a new qubit with a known state from the ancilla. Lockyer et al.[34] proposed and synthesized (as in Figure 1.5 a)) a molecule with a $S = 1/2$ Cr_7Ni ring coupled via an exchange interaction to a Cu ion, composed of an electronic spin coupled by hyperfine interaction to the $I = 3/2$ nuclear spin. In this scheme (as in Figure 1.5 b)), the Cr_7Ni qubit serves as a processor, the electron spin is an ancilla qubit as in panel c) in Figure 1.5, and the nuclear qudit acts as the quantum memory, respectively[34].

1.4.4 Defects Qubits

Point defect with spins in solids constitute a two-level system and are considered essential building blocks for application in QC and sensing when the electron spin can be initialized and read out with sufficiently long coherence time. The nitrogen-vacancy (NV) centre in diamond has been already identified as a qubit that can be exploited in diverse quantum technology applications[35]. The NV qubit state is initialised and read out by optical means in which spin-photon interface can be realized for quantum communication in the visible wavelength region. However is technologically very challenging to develop a scalable fabrication and optical waveguide integration of NV centers.

Compared to qubits in 3D materials like NV, defects in two-dimensional (2D) have wide bandgap host and distinguish themselves with high quantum efficiency and additional functionalities due to
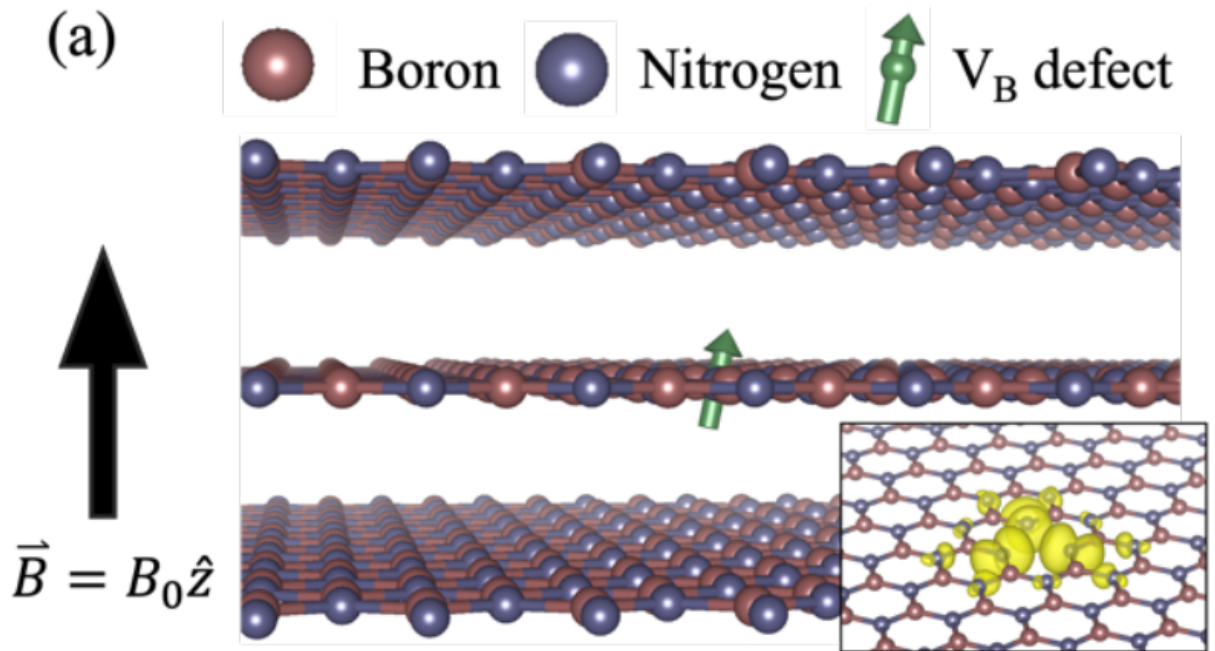
Figure 1.6: Proposal for vacancy spin in hBN[36].

spatial confinement and near-surface location. For this reason there has been various other proposals such as hBN (hexagonal Boron Nitride) with Boron vacancy (V_B^-), exemplified in Figure 1.6, in which possible qubit states were envisaged as the triplet sublevel systems of the vacancy and the read-out as ODMR (Optically Addressed Magnetic Resonance)[36].
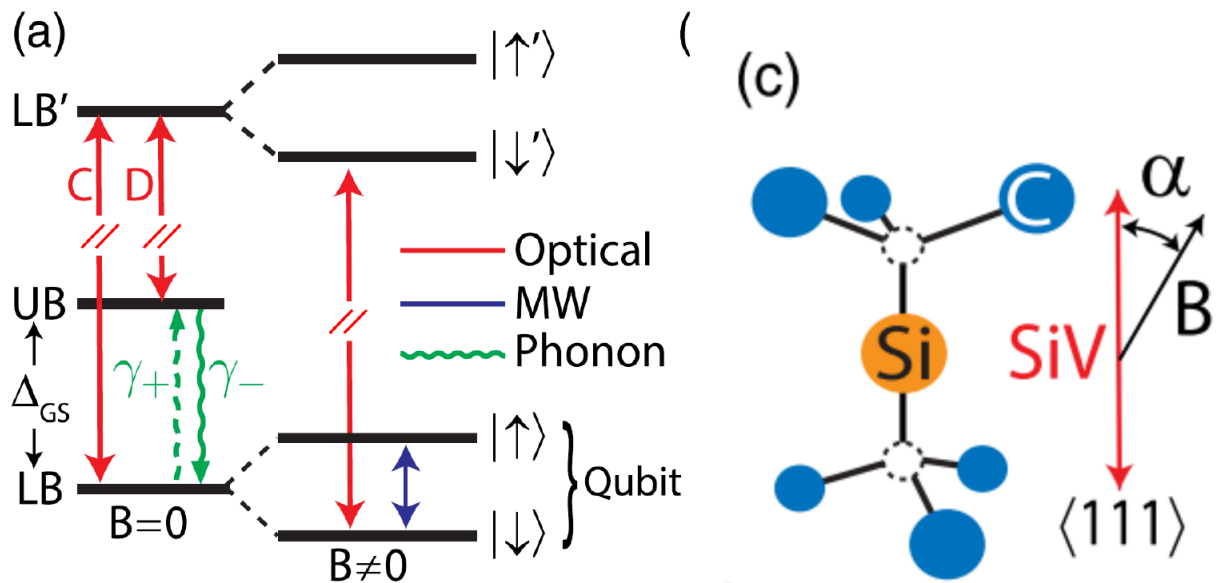
Figure 1.7: Proposal for silicon vacancy in diamond. In panel a): representation of energy levels for the possible qubit. On panel c): crystal representation of the Si vacancy in diamond.[37].

A variation of what it was previously seen in has been made with silicon vacancies in diamond as in Figure 1.7. This kind of system proposed can have coherences of tens of ms and can be used as quantum memories that are really needed in this field. The qubits are identified as the states in the Lower Band (LB), that is the maximum valence band for a solid material (we will explain deeper the meaning of this affirmation), splitting of the spin states. The readout is realized through optical

or microwave laser regime[37].
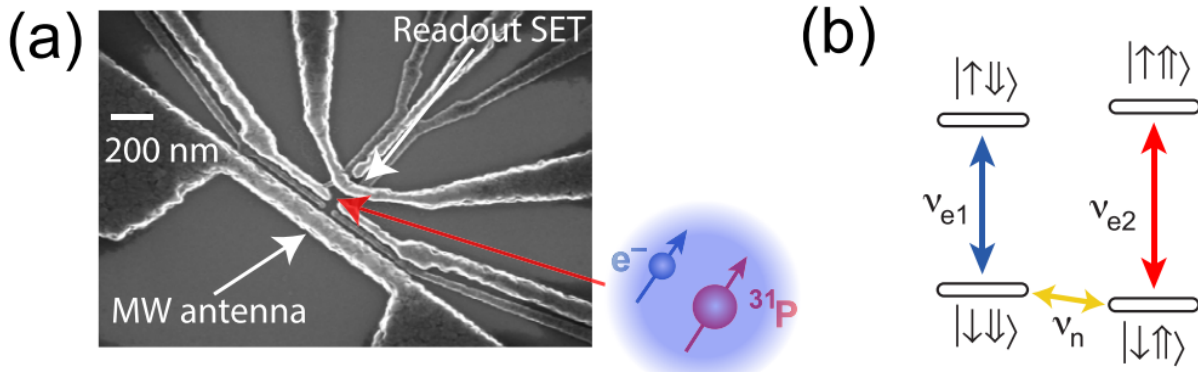
Figure 1.8: Proposal for phosphorus vacancy in Silicon matrix. On panel a): SET image of the setup proposed. On panel b): representation of energy levels in [31]P.[38].

A further example of defected system can be seen in Figure 1.8 where we have a ^{31}P defect in a Silicon matrix. The qubit are defined as the electronic and nuclear states of the phosphorus atom. The readout is made possible mainly through optical regime[38].

1.5   Why 2D materials with defects?

As we discussed in the previous sections, defects in a host (like NV centers) were one of the first few materials that were studied thoroughly in literature, due to the fact that they exhibit a long coherence time of the qubits even at room temperature. Since TMDs have very peculiar properties and since the defects in 2D materials are relatively stable we envisage that a defect (Carbon for example) in a 2D material host (a suitable TMD) can open up new options in the landscape of solid state qubits. There were already proposals of this kind and we would like to level up the understanding of these types of materials through an ab-initio analysis of their properties to further investigate one that seems to fit the best the DiVincenzo requirements.

1.5.1   An example of defected material for quantum computing

What we aim here is to describe a theoretical proposal from Li Song et al.[39]. They studied a monolayer of WS_2 with a carbon defect that substitutes one of the sulphur atom in the lattice as in panel a) Figure 1.9. They studied the properties of such systems both in the case of a charged carbon atom and a neutral one (with state depicted in panel b) Figure 1.9). What is interesting about this study is the proposal for a quantum protocol that could possibly work respecting the Di Vincenzo criteria. Let us analyse the protocol shown in Figure 1.9. The quantum protocol starts with an optical pumping of electrons. In the c) panel of Figure 1.9 we can see the ground state denoted as ^1A that is excited to the state ^1E. The electrons in the excited state rapidly undergo an Inter-System-Crossing (ISC) into the ^3E state composed of three degenerate pairs of states (6 in total). After a discussion on the role of the SOC and the Jahn-Teller effect the researchers analyse a subset of
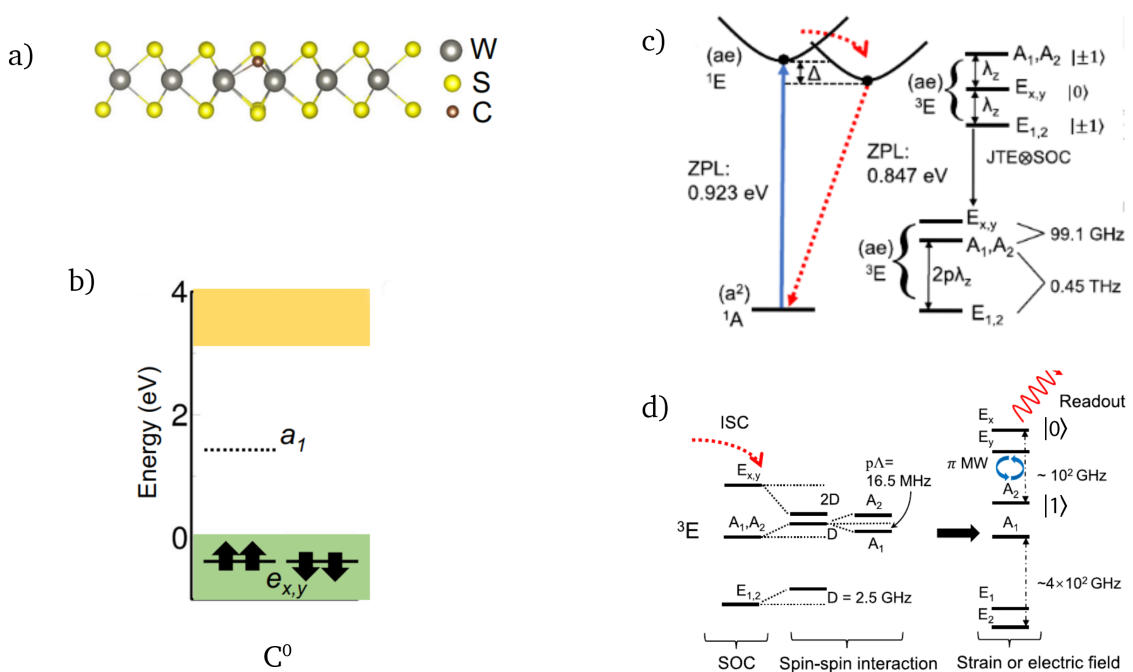
Figure 1.9: Picture depicting structure of the WS_2@C, energy levels of the carbon atom and the fine structure of energy levels. In a) we can find side view of the defect substituting the sulphur atom. In c) we can find the level structure represented that roughly describes the states of carbon defect in material. The green and yellow zones are the valence and conductance bands respectively. c) and d) are the representations of electronic structure of the system without and with applied strains respectively. Adapted from Ref. [39]

separated states as pictured in panel d) Figure 1.9. Since the ISC is quick, most of the population of electrons pumped in, will be localized in the top E_x state. When radiation in the microwave region is shine on the material, a photon will be emitted from such a state and thus giving us a read of the state $|0\rangle$. When instead the population in E_x is low and part of the population is high in the A_2 state a photon will be absorbed giving us a reading of the state $|1\rangle$.

The researchers used mainly high theory level in order to run these type of calculations. These algorithms are suitable for in depth analysis of the electronic structures, but are very demanding in terms of computational resources. We took inspiration from this paper to find a more efficient way to run some of their calculations. This is done in order to develop a high-throughput screening on many different materials and find the most suitable to be investigated with more advanced techniques.

1.6 Goals and future perspectives

The goal of this thesis is to reproduce some specific features of TMDs using a "low-cost" computational protocol, for example calculating the direct transition from the ground state to different excited states, comparing it with what we find in the literature. The protocol is implemented as a custom made script written in BASH (Bourne Again SHell) to interface with Quantum Espresso [40] (a suite that exploit the DFT theory). We used this suite because it is open source and easy to interface

with other scripting languages in order for our protocol to be automatized. Even if we tested the code on only two materials it was built with the purpose of being adapted to various materials. If our code turn to be accurate as the literature reference but perform better in term of computational cost and time, this will become the core of the screening routine that will analyse many different materials and defects. In order to do this one can expand the research beyond the two materials that we will analyse later, including for example different defects (substituting S with N, P; etc. or changing some transition metal from W to Re ...). In this way we will have a plethora of different materials and we will screen them in parallel (also known as HTS, High-Throughput-Screening) in order to find the most suitable to host a qubit or maybe multiple qubits. But this will require the identification of key parameters for the qubit goodness, like decoherence time, initialization protocols, etc. The natural perspective of this thesis will be to implement all of the above procedures to simulate a multi-qubit material and see how these defect, that generate the qubits, behave under ideal conditions and if they interact sufficiently to create an entangled pair state.

Theoretical Methods

In this section we will discuss the theoretical framework used to calculate the properties of our systems, namely MoS_2 and WS_2 with carbon as defect. We will introduce the basics of Density Functional Theory (DFT) and see how can be used as a probing theory in finding new potential candidate for Quantum Computing. We will discuss the role of the exchange-correlation (xc) functionals that can give us a glimpse into the electronic structure of these materials. We will discuss the Kohn-Sham equations and the Hohenberg and Kohn Theorem. Then we will use the main result from the Bloch theorem to understand how plane-wave calculations differ from localized basis one. Subsequently we will talk about the role of the pseudopotentials in our calculations and the different types often used and the band-gap problem and where it does come from. We will also explain how the Density Of States (DOS) is calculated, what is the Projected Density Of States (PDOS) and how they are useful diagnostic tools. Finally we will analyze the importance of the Spin Orbit Coupling, moving on to describe what is a ΔSCF method and finally talking about the formation energy. We will now describe the main problem and how to tackle it.
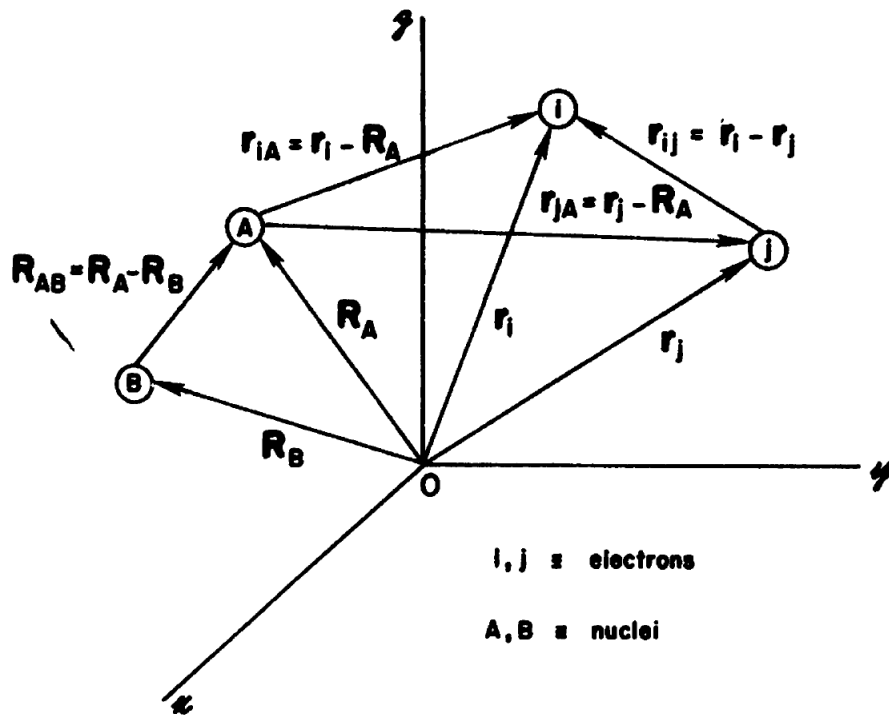
Figure 2.1: A hydrogenoid system in which *i* and *j* are electrons and *A* and *B* are nuclei

2.1 The many-body quantum problem

The fundamental problem to tackle here is to find an approximation for the solutions of the time-independent Schroedinger equation:

$$\mathcal{H} \left| \Phi \right\rangle = \varepsilon \left| \Phi \right\rangle , \qquad (2.1)$$

where $\mathcal{H}$ is an hamiltonian operator for a system of nuclei and electrons (their positions are respectively described by $\boldsymbol{R_A}$ and $\boldsymbol{r_i}$ like in Figure 2.1). The distance between the *i*-th electron and *A*-th nucleus is $r_{i,A} = \mid \boldsymbol{r_i} - \boldsymbol{R_A} \mid$; the distance between the *i*-th and *j*-th electron is represented by $r_i = \mid \boldsymbol{r_i} - \boldsymbol{r_j} \mid$; moreover the distance between the *A*-th nucleus and the *B*-th is $R_{AB} = \mid \boldsymbol{R_A} - \boldsymbol{R_B} \mid$, see Figure 2.1. Using atomic units, the energy of a system of *N* interacting electrons and *M* nuclei in a solid can be described by the formula[41]:

$$\mathcal{H} = -\sum_{i=1}^{N} \frac{1}{2} \nabla_i^2 - \sum_{A=1}^{M} \frac{1}{2M_A} \nabla_A^2 - \sum_{i=1}^{N} \sum_{A=1}^{M} \frac{Z_A}{r_{iA}} + \sum_{i=1}^{N} \sum_{j>i}^{N} \frac{1}{r_{ij}} + \sum_{A=1}^{M} \sum_{B>A}^{M} \frac{Z_A Z_B}{R_{AB}} \qquad (2.2)$$

The first two terms in this Hamiltonian refer respectively to the kinetic energy of the electrons and nuclei respectively, then there is the Coulomb interaction between electrons and nuclei, finally the last two represent the repulsion between electrons and nuclei respectively.

We could minimize the expectation value of the operator in Equation 2.2 and find the related approximated eigenvalues for the problem, but this is quite a daunting task and we will rather prefer some more insightful approximation to the problem.

As a first step we can recognize that the electron mass is a 1836-th of that of the proton. Thus we can assume that the dynamics of the electrons adapt instantaneously with the position of the single nuclei that can be considered still when we focus on the electron's momenta. This allows us to decouple the ionic and electronic degrees of freedom: this is the well known Born-Oppenheimer (BO) approximation. Within the BO approximation we can write our hamiltonian in[41]:

$$\mathcal{H} = -\sum_{i=1}^{N} \frac{1}{2} \nabla_i^2 - \sum_{i=1}^{N} \sum_{A=1}^{M} \frac{Z_A}{r_{iA}} + \sum_{i=1}^{N} \sum_{j>i}^{N} \frac{1}{r_{ij}} = T + V_{ext} + V_{e-e} \tag{2.3}$$

and even though we have simplified the problem, finding its eigenstates and eigenvalues is still a hard task. We will thus shift focus and concentrate on instead another quantity, the total electronic density $n(\vec{r})$ that can be written as $N \int \psi^*(\vec{r}, \vec{r}_2, \ldots, \vec{r}_n) \psi(\vec{r}, \vec{r}_2, \ldots, \vec{r}_n) d\vec{r} d\vec{r}_1 \ldots d\vec{r}_n$ (where N is a normalization factor and ψ are our multi-electronic wavefunctions) instead of a complicated many-body wavefunction $\Psi(r_1, \ldots, r_N)$. This pave the way into studying molecules and finite systems with limited computational resources[42].

2.2 Kohn-Sham equations and Hohenberg and Kohn Theorem

Density Functional Theory (DFT) was first conceived by Hohenberg and Kohn in their seminal paper [43] that treats the case of the ground state of an interacting electron gas in an external potential.

The Hohenberg and Kohn theorem states that once the mutual interaction among electrons is fixed, in a non time dependent picture and assuming that all the potentials acting on the system are local, then the knowledge of the ground state density and that of the complete Hamiltonian are completely equivalent informations. Thus the Hamiltonian is completely determined by it's ground state density and the viceversa. Said in another way:

> *The ground state expectation value of any observable (including the ground state energy) is a unique functional of the exact ground state density*

and also that:

> *In particular, the energy functional, once the external potential is specified, finds it minimum at the ground state density of the system*[43]

Now, we will not find the energy as a real number directly from our computation. Using an Hamiltonian, like in Equation 2.3, we will seek for the function that actually minimizes the energy, and this is called a functional. A functional can be described as a function whose argument is itself a function. So if $f(x)$ is a function and F is a functional then $F[f(x)]$ returns a scalar value that is what we are interested in.

So if we write our ground state energy as a functional of our ground state density n expressed as $E = E[n]$.

Now if we fix the external potential (generated by the nuclei) $v = v_0$ we know from the propositions that the ground state density n_0 corresponds univocally to this potential. Since all the possible wavefunctions that are linked to all possible densities $\mathcal{N}$ does not depend on the specific choice of v_0 the variational principle yields to:

$$E_0 = E_{v_0}[n_0] = \min_{n \in \mathcal{N}} E. \tag{2.4}$$

Another important consequence of this fact is that we can divide the total energy functional into two parts:

$$
\begin{aligned}
E_{v_0}[n] &= \langle \psi[n] | \, T + V_{e-e} + V_0 \, | \psi[n] \rangle \\
&= \langle \psi[n] | \, T + V_{e-e} \, | \psi[n] \rangle + \int V_0(r) n(r) d^3 r \\
&= F_{HK} + \int V_0(r) n(r) d^3 r
\end{aligned}
\tag{2.5}
$$

where F_{HK} is a universal functional of n, not depending on the choice of V_0.

In this way we have found a method to obtain the ground state energy, not from the original hard Equation 2.1, but translating its information inside a functional $E[n]$ that's easier to handle and for which there are known methods of minimization with respect the density $n(r)$. The problem here is that the general form of $E[n]$ is not know *a priori* but we can have some hint on where care should be put in order to use DFT properly.

2.3   Single particle scheme, approximations and plane wave methods

With the paper by Kohn and Sham [44] there as been a breakthrough where the authors introduced ad hoc terms to the contribution of the total energy E, like E_{xc} in Equation 2.6. There were two main advantages with this approach: first, it provides a single particle scheme to obtain the ground state energy, and second, to have an expression in which the approximations to the unknown part would be not so drastic. We can write, in the KS scheme, the total energy functional of the interacting system as:

$$E[n] = T_{KS}[n] + E_H[n] + \int n(\vec{r}) V_{ext}(\vec{r}) d\vec{r} + E_{xc}[n] \tag{2.6}$$

where $T_{KS}[n]$ is the kinetic energy of a non-interacting system with density defined by n, v_{ext} is

the external potential generated by the nuclei, E_H is the Hartree contribution to the total energy:

$$E_H[n] = \frac{1}{2} \iint \frac{n(r)n(r')}{|r - r'|} d^3r' d^3r \tag{2.7}$$

and E_{xc} is the remaining part of the energy including the exchange-correlation term and the difference between T and T_{KS} respectively for the kinetic energy of the N-electron system and for the non-interacting system. It is the last term indeed that introduce the idea of studying a simpler, fictitious, non-interacting system instead of a complicated interacting system. The Hamiltonian for the fictitious system can be written as:

$$\left[-\frac{1}{2}\nabla^2 + V_{ext} + V_H + V_{xc} \right] \phi_i(\vec{r}) = \varepsilon_i \phi_i(\vec{r}), \tag{2.8}$$

where $V_{xc} = \frac{\delta E_{xc}[n]}{\delta n}$ is the exchange-correlation potential of the interacting system. By construction the same ground state density of the interacting system can be written as:

$$n(r) = \sum_i f_i |\phi_i(\vec{r})|^2, \tag{2.9}$$

f_i being the occupation number of the state i.

It is now possible, given an approximation of $E_{xc}[n]$, to solve the Kohn-Sham equations self consistently and calculate the density of the real system via Equation 2.6. Once the density is known, it is possible to calculate the energy of the ground state of the interacting system and hence, by proper minimization, to find its ground state geometry.

2.3.1 The exchange-correlation potential and functional

Comparing Equation 2.5 and Equation 2.6 we can see that the exchange-correlation energy is defined as:

$$E_{xc}[n] = E_{HK}[n] - T_{KS}[n] - E_H[n] =$$
$$= T_{HK} + \langle \Psi[n] | V_{e-e} | \Psi[n] \rangle - T_{KS} - E_H[n] \tag{2.10}$$

where $\Psi[n]$ is the GS wavefunction. ϕ_{KS} is the Kohn-Sham wavefunction that is obtained in the self consistent scheme and it is usually a single Slater determinant. T_{HK} is the kinetic energy of the real system, the expectation value of the kinetic energy operator on the state $\Psi[n]$.

We can divide E_{xc} in two parts:

$$E_{xc}[n] = E_x[n] + E_c[n]. \tag{2.11}$$

The exchange energy E_x is defined following an Hartree-Fock like definition, as:

21

$$E_x[n] = \langle \phi_{KS} | V_{e-e} | \phi_{KS} \rangle - E_H[n] \tag{2.12}$$

It has to be noted that the exchange energy corrects the spurious self-interaction present in the Hartree energy, like the Fock term does in the Hartree-Fock scheme. The correlation energy E_c is defined as the difference between E_{xc} and E_x, thus comparing Equation 2.10 and Equation 2.12 and substituting in Equation 2.11 we obtain:

$$E_c[n] = \langle \Psi[n] | T + V_{e-e} | \Psi[n] \rangle - \langle \phi_{KS} | T + V_{e-e} | \phi_{KS} \rangle. \tag{2.13}$$

We know that $\Psi[n]$ minimises the total energy of the interacting system, thus $E_c[n] < 0$. On the other hand ϕ_{KS} minimise the total energy of the non-interacting system and thus we know that $\langle \Psi[n] | T | \Psi[n] \rangle - \langle \phi_{KS} | T | \phi_{KS} \rangle > 0$. So $E_c[n]$ is the sum of a positive kinetic energy contribution and a negative potential contribution, which prevails.

Since it is analytically unknown, the main problem in DFT is to find a good approximation for the exchange-correlation (XC) functional. Despite it gives a small contribution with respect to the others in term of energy, it influences the ground state charge density and the global energy up to 10-20% of the real value. Fortunately, this functional can be reasonably approximated by a local or almost-local functional of the density.

The first and simplest approximation on $E_{xc}[n]$ was introduced by Kohn and Sham and was called the Local Density Approximation (LDA)[44]. It assumes that the XC energy of a real system behaves locally as an homogenous electron gas, whose energy is well known[45]. This XC functional can be expressed as:

$$E_{XC}^{LDA}[n(\vec{r})] = \int n(\vec{r}) \varepsilon_{XC}^{HOMO}(n(\vec{r})) d^3\vec{r} \tag{2.14}$$

where $\varepsilon_{XC}^{HOMO}(n(\vec{r}))$ indicates the energy of the homogenous electronic gas. Usually, LDA calculations can closely reproduce vibrational and structural properties of strongly bound systems but often tend to overestimate binding energies while underestimating bond lengths.

The natural evolution of LDA was the Generalized Gradient Approximation (GGA) in which the local XC energy depends not only from $n(\vec{r})$ but also on his gradient $\vec{\nabla} n(\vec{r})$, becoming:

$$E_{XC}^{GGA}[n(\vec{r})] = \int n(\vec{r}) \varepsilon_{XC}^{HOMO}(n(\vec{r}); \vec{\nabla} n(\vec{r})) d^3\vec{r} \tag{2.15}$$

GGA significantly improves upon LDA to simulate the binding energies of real molecules. A GGA functional adopted in this thesis is the BP86 functional which is composed of the Becke 88 exchange[46] and Perdew 86 correlation functional[47].

Another class of widespread XC functionals is the so-called hybrid functionals where the ex-

change energy, calculated in an exact manner (i.e. Hartree-Fock method), is mixed with those obtained by DFT. An example of hybrid functional employed in this work is B3LYP, which is composed by parametrized B3 exchange functional, which uses 3 parameters to mix the exact Hartree-Fock exchange term, and LYP functional that supply the electrons correlation[48].

2.3.2   Energy cutoff and K-point sampling

Since we will deal with a crystalline solid we will use the results from the Bloch theorem[49] as a starting point for our discussion. In a periodic system each electronic eigenfunction can be written as the sum of plane waves:

$$\psi_{n,k}(\vec{r}) = \sum_{\vec{G}} c_{n,\vec{k}+\vec{G}}\, e^{i(\vec{k}+\vec{G})\cdot\vec{r}}, \tag{2.16}$$

where $\vec{G}$ are the reciprocal lattice vectors and $\vec{k}$ is a vector in the first Brillouin zone of the material. K-points are sampling points in the first Brillouin zone which is the specific region of reciprocal-space which is closest to the origin. The KS equation now has a simpler form: the Hamiltonian for each k-point is a matrix in the reciprocal space $(\vec{G}, \vec{G}')$; and one should diagonalise it in order to get the coefficients of the planewaves.

Bloch's theorem states that the electronic wavefunctions at each k-point can be expanded in terms of a discrete plane-wave basis set. In principle, an infinite number of plane waves is required for such an expansion. However the coefficients $c_{\vec{k}+\vec{G}}$ for the plane waves with small kinetic energies,$|\vec{k}+\vec{G}|^2$, are more important than those with large kinetic energies. Thus, the plane wave basis set can be truncated to include only plane waves that have kinetic energies that are smaller than some particular cutoff energy E_{cut} [50]:

$$\frac{1}{2}|\vec{G}|^2 \leq E_{cut} \tag{2.17}$$

$\vec{G}$ and $\vec{k}$ in principle are infinite, but this would mean we have to implement infinite summations in the code, something that is not possible to do. What actually is done is to sample the Brillouin zone with a finite grid of points and to introduce a cutoff in the kinetic energy that limits the summation over the $\vec{G}$ vectors. Since we are dealing with materials very similar to each other the energy cutoff can be left unchanged.

In fact if two close wavefunctions in the $\vec{k}$ space are nearly identical with each other we can assume safely that one of those wavefunctions can represent the entire region of the Brillouin zone. Of course we need convergence over the number of $\vec{k}$ points. However there are special sets of $\vec{k}$ points for which, exploiting the symmetry of the system, very accurate calculations can be performed with a reasonable small number of $\vec{k}$ points.

Moreover even the electron density can be expanded on G:

$$n(\vec{r}) = \sum_{\vec{G}} n(\vec{G}) e^{i\vec{r}\vec{G}}. \tag{2.18}$$

2.3.3 Discussion on pseudopotentials

The pseudopotential is an attempt to replace the complicated effects of the motion of the core (i.e. non-valence) electrons of an atom and its nucleus. Normally, in the Kohn-Sham equation, the potential term is expressed as a Coulombic potential, but its usually substituted with a pseudopotential in order to describe better the valence electrons than the core ones[51]. The form of the energy functional is not the only approximation that is typically used in plane wave ab-intio calculations. The pseudopotentials are used to model the interaction between the positive ion and the electrons in order to eliminate: the singularity of the electrostatic potential of the nuclei, the very localised core electrons and the nodes of the valence electrons close to the nuclei. The idea arises from the experience that the core electrons are never predominant in the chemical bond, and thus the wavefunction describing these electrons is practically the same in different chemical environments. Since the global effect of these core electrons is to push away the electrons of the outer shells from the nuclei, their presence can thus be compared to a repulsive potential. If we sum these contributions with the ones from the nuclei this produces a much weaker potential.

Common employed pseudopotentials are the so-called norm conserving and ultrasoft. The norm conserving pseudopotentials give the mathematical warranty that the inner electrons pseudo-charge is equal to the real charge and that provides an efficient approach in many simulations cases. On the other side, ultrasoft pseudopotentials relax the norm-conserving behaviour and the orthonormality of the atomic orbitals in order to reduce the basis-set size, i.e. the number of plane-wave in our case. This is very convenient in systems which require large basis set and have proved to be very accurate in the description of big system properties. In this work, we will use a UltraSoft PseudoPotential (USPP) to simulate our materials .

2.4 The Bandgap problems

We will now delve into the details of where does the band-gap problem arise in DFT. This is a known problem in DFT which is prone to underestimate the band-gap of a system, resulting in bad estimates for transition energies and other related problems.

Even though the agreement with experiments are quite good it's important to understand that that changing the functional can, in principle, lead to a better description of the band structure within the Kohn-Sham scheme. Often the bandgap in the DFT at PBE level underestimate the magnitude of the gap. We will see why, but it will be important to get insights on the physical content of the Kohn-Sham eigenvalues.

There has been proposed an extension to the DFT formalism to fractional number of states by defining proper energy functionals for statistical mixtures. [52] In this framework the ground state energy of $(N+\omega)$-particle state described by the corresponding statistical mixture with $N \in \mathbb{Z}$ and $\omega \in [0, 1]$ is given by:

$$E_{gs}^{N+\omega} = (1 - \omega)E_{gs}^N + \omega E_{gs}^{N+1}. \tag{2.19}$$

From the equation above, while E_{gs}^N is a continuous function of N, its derivative, the chemical potential $\mu = \frac{\partial E}{\partial N}$ might be discontinuous as the variable N assume an integer value. It was also shown that:

$$\frac{\delta E^N[n]}{\delta n(r)} = \frac{\partial E}{\partial N}\bigg|_{N-\delta} = \mu^- \tag{2.20}$$

where δ is a positive infinitesimal quantity, and by μ^- we mean the left limit of μ. The last equation states that the left limit of the chemical potential is correctly given by the functional derivative of the total energy functional of an N-particle calculation.

Another theorem by Janak [53] states also that the partial derivative of the total energy functional with respect to the occupation of some KS state is given by the same KS-eigenvalue:

$$\frac{\partial E}{\partial f_i} = \varepsilon_i. \tag{2.21}$$

So comparing the last two equations we can clearly see that within DFT the left limit chemical potential is given correctly by the energy of the highest KS occupied state:

$$\mu^- = \varepsilon_N^{(N)}. \tag{2.22}$$

From the last equation it is also straightforward to reckon that the ionisation potential $I(N)$, and the electron affinity $A(N)$ are given by:

$$I(N) = E_{N-1} - E_N = -\int_{N-1+\delta}^{N+\delta} \frac{\partial E}{\partial N} dN = -\mu^-(N) = -\varepsilon_N^{(N)} \tag{2.23}$$

$$A(N) = E_N - E_{N+1} = -\int_{n+\delta}^{N+1+\delta} \frac{\partial E}{\partial N} dN = -\mu^+(N) = -\mu^-(N+1) = -\varepsilon_{N+1}^{(N+1)} \tag{2.24}$$

The electronic gap thus can be defined as the difference between ionization potential and electron affinity:

$$E_g = I - A = -\varepsilon_N^{(N)} + \varepsilon_{N+1}^{(N+1)} \tag{2.25}$$

This sets a connection between the true gap and the difference in energies in between the highest

occupied states and the lowest occupied one. Now, how is this connected to the Kohn-Sham gap, namely $E_g^{KS} = -\varepsilon_N^{(N)} + \varepsilon_{N+1}^{(N+1)}$? From the expression for the true gap:

$$E_g = \mu^+(N) - \mu^-(N) = \left(\left.\frac{\delta E[n]}{\delta n}\right|_{N+\delta} - \left.\frac{\delta E[n]}{\delta n}\right|_{N-\delta} \right) \tag{2.26}$$

only terms arising from the kinetic and exchange correlation part of the total energy functional might contribute to this expression. The remaining part will give a null contribution since, in extended systems, like those inherently described by plane waves, the addition of one electron is an infinitesimal perturbation, and the change in the density is null being the volume infinite. Taking this into account,

$$E_g = \left.\frac{\delta T}{\delta n}\right|_{N+\delta} - \left.\frac{\delta T}{\delta n}\right|_{N-\delta} + v_{xc}^+ - v_{xc}^-. \tag{2.27}$$

Now let us consider the Kohn-Sham system: it is a system of free particle moving in an effective potential v_{xc}. Therefore the electronic gap is given by the discontinuity of the kinetic part of the energy functional, so that:

$$E_g^{KS} = \left.\frac{\delta T}{\delta n}\right|_{N+\delta} - \left.\frac{\delta T}{\delta n}\right|_{N-\delta} \tag{2.28}$$

Comparing now the last two equations we can see that the KS-DFT gap E_g^{DFT} of the N particle system, is related to the true quasiparticle gap through the discontinuity Δ of the exchange and correlation potential when an electron is added to the system.

$$E_g = E_g^{KS} + \Delta = \varepsilon_{N+1}^{(N)} - \varepsilon_N^{(N)} + v_{xc}^+ - v_{xc}^-. \tag{2.29}$$

Now, if Δ is very small, a good enough functional would provide the correct gap; viceversa, if Δ is big, no matter how good the functional is, the Kohn Sham gap cannot provide a good approximation for the quasiparticle gap. The problem of quasiparticle energies should then be addressed by other theories.

2.5 What is the Density of States

The DOS and PDOS are useful diagnostic tools for us to be sure that the defect is indeed present in the structure that we have simulated and to estimate the relative position of the energy levels of the defect inside the bandgap between the two materials. The density of states gives the number of allowed electron (or hole) states per unit volume at a given energy. The calculation of some electronic processes like absorption, emission, and the general distribution of electrons in a material requires us to know the number of available states per unit volume per unit energy. The density of states is represented by a function $g(E)$ which is a function of the energy and has the relation

$g(E)dE = \frac{\#(states)}{unitvolume}$ in $(E, E + dE)$. Taking a step back, we look at the free electron, which has a momentum, p and velocity, v , related by $p = mv$. The energy of a free electron is entirely kinetic and thus we can disregard the potential energy term and say that the energy is $E = \frac{1}{2}mv^2$. Recalling the De Broglie's wave-particle duality we have that an electron has an assigned wavenumber k that relates to it by the momentum divided by the reduced Planck constant: $k = \frac{p}{\hbar}$. If we substitute the momentum expression into the De Broglie relation we obtain:

$$k = \frac{p}{\hbar} \Rightarrow k = \frac{mv}{\hbar} \Rightarrow v = \frac{\hbar k}{m} \tag{2.30}$$

substituting then the kinetic energy term:

$$E = \frac{1}{2}m\left(\frac{\hbar k}{m}\right)^2 \Rightarrow E = \frac{1}{2}\frac{\hbar^2 k^2}{m^*} \tag{2.31}$$

we then obtain what is known as the dispersion relation for a free electron in Equation 2.31. We can picture the allowed values from Equation 2.31 as a sphere in K-space centered at the origin with a radius k and thickness dk. The allowed states are now found within the volume contained between $(k, k + dk)$. We define the density of states per unit volume as: $\rho'(k) = \rho(k)/V = \frac{k^2}{2\pi^2}$ and since for each k we can have two possible electronic wavefunctions with opposite spin we have:

$$g(E)dE = 2\rho'(k)dk = \frac{k^2}{\pi^2}dk \Rightarrow g(E) = \frac{k^2}{\pi^2}\left(\frac{dE}{dk}\right)^{-1} \tag{2.32}$$

substituting Equation 2.31 in the last one, rearranging and deriving the terms, we arrive at:

$$g(E) = \frac{1}{2\pi^2}\left(\frac{2m^*}{\hbar^2}\right)^{\frac{3}{2}} E^{\frac{1}{2}}. \tag{2.33}$$

The Equation 2.33 tell us that the DOS scales with the square root of the energy, moreover it is proportional to the power of $3/2$ of the effective mass of the electrons. The effective mass depends on the curvature of the energy with respect to k: $m^* = \hbar^2(\frac{\partial^2 E}{\partial^2 k})^{-1}$ [49]. This is in fact the behavior that we would obtain from a bulk solid in 3D. Starting with different geometries of the volume we would obtain slightly different equations and these are depicted in Figure 2.2 panel a).

In panel b) of Figure 2.2 we have an example of a quantum dot geometry and its relative expression. We will find the same functional behavior in the DOS results for the defected system in the third chapter.

Another interesting point of the DOS is that it reflects some of the properties found in the band structure graph. This means that if we have a gap (E_g) in the band structure (Figure 2.3 left panel) we will see the same energy gap even at the level of the DOS and viceversa. Instead if we have no gap (Figure 2.3 right panel) in the band structure (e.g. in a metal) we will not see any gap neither at the level of DOS nor in the band structure [54].
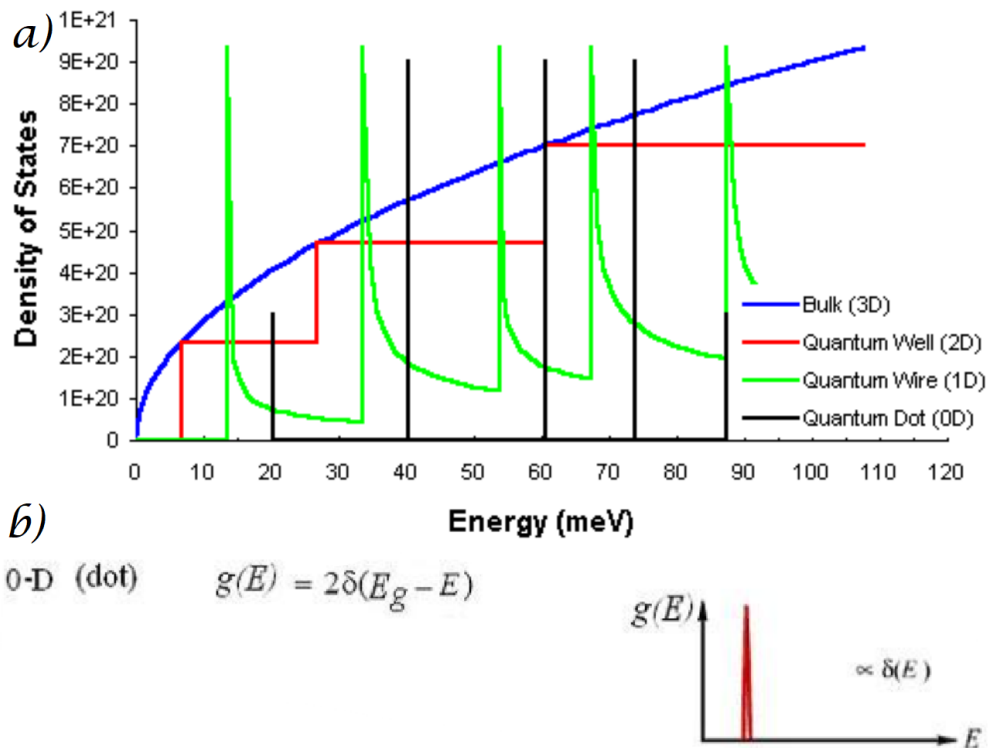
Figure 2.2: In panel a) we have different DOS graph for different starting geometries. In panel b) we have an example of a 0 dot geometry in detail.
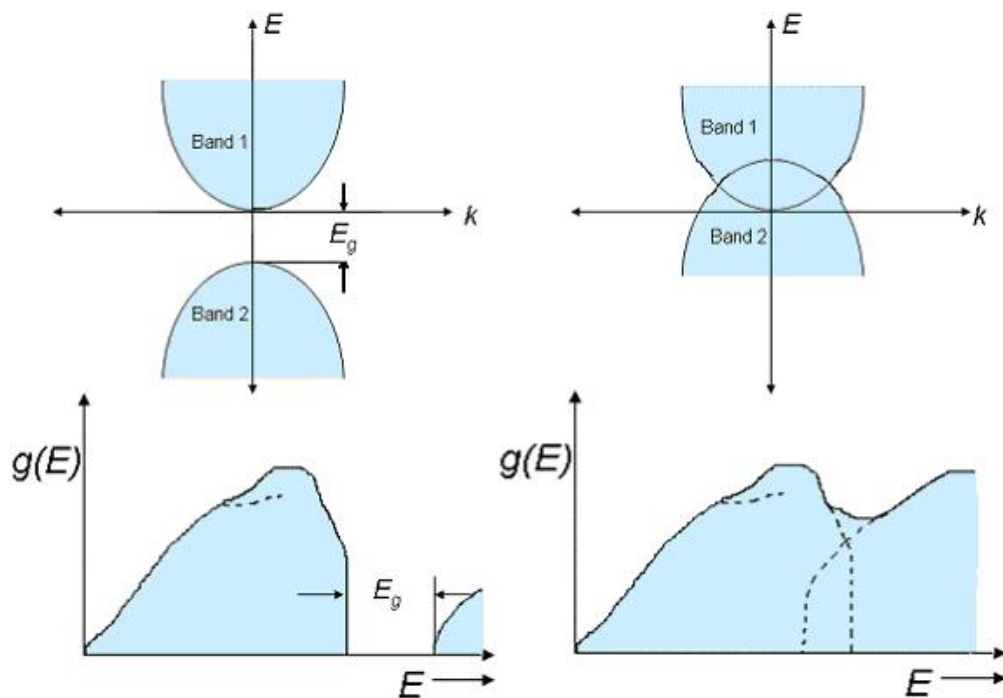
Figure 2.3: The left hand side shows a two-band diagram and a DOS vs. E plot for no band overlap. The right hand side shows a two-band diagram and a DOS vs. E plot for the case when there is a band overlap.

We can in general project the DOS onto some specific atomic orbitals. This is called the Projected Density Of States (PDOS). So, if we sum over all the projections, we will have the total density of state, or simply, the DOS. These are useful tools to obtain information and insight relevant to important applications. For example, in the field of heterogeneous catalysis, the density of states projected onto the d-band at metallic surfaces is a powerful descriptor of a surface's bonding ability, which can be used to estimate its efficiency as a catalyst for a given reaction[55].

The PDOS can be calculated starting from the number of one-electron levels with weight on

28

orbital μ between the energy E and $E + dE$ called $g_\mu(E)dE$ as in:

$$g_\mu(E) = \frac{1}{N_{\vec{k}}} \sum_i^{bands} \sum_{\vec{k}} \sum_\nu c_{\nu i}^*(\vec{k}) c_{\mu i}(\vec{k}) S_{\nu \mu}(\vec{k}) \delta(E - E_i(\vec{k})) \qquad (2.34)$$

where $c_{\nu i}^*(\vec{k})$ and $c_{\mu i}(\vec{k})$ are the coefficients of the eigenvector $\psi_i(\vec{k})$ with eigenvalues $E_i(\vec{k})$, $S_{\nu \mu}(\vec{k})$ is the overlap matrix of the atomic basis of choice and $\delta(E - E_i(\vec{k}))$ is a delta function describing the particular DOS of the system.

The link between the DOS and PDOS is given by the formula:

$$g(E) = \sum_\mu g_\mu(E) \qquad (2.35)$$

2.6   Isosurfaces

Wave functions that are solutions to Schrödinger's equation for the hydrogen atom are called orbitals. When it comes to orbitals, we need the knowledge of: shape, spatial extent (i.e., how far from the nucleus an orbital penetrates space), phase (i.e., the sign of the wave function in different regions of space), and energy.

Every point in space, $\psi(x, y, z)$, takes on a particular numerical value. Thus, to represent the value of ψ everywhere in space we would require a fourth dimension. To deal with this problem a particular numerical value of ψ is chosen and connect all the points in space that have this value. The result is called an isosurface, and it represents the shape of the orbital. Shading (or color) is used to represent the sign of the wavefunction.

However when we calculate the solutions to the Schrödinger equation, in a periodic potential, the solutions take the form of a plane wave modulated by a periodic function:

$$\psi_{n\vec{k}} = e^{i\vec{k} \cdot \vec{r}} u_n(\vec{r}) \quad with \quad \psi_{n(\vec{k}+\vec{K})} = \psi_{n\vec{k}} \qquad (2.36)$$

where $\psi_{n\vec{k}}$ is an eigenstates in which n is a discrete index, called the band index, which is present because there are many different wave functions with the same $\vec{k}$, and the condition $\psi_{n(\vec{k}+\vec{K})} = \psi_{n\vec{k}}$ tell us that the eigenstate are uniquely defined up to a constant in the reciprocal lattice. This leads to the problem that, to plot the isosurfaces of the orbitals with their relative phase, we need to keep the constant $e^{i\vec{k} \cdot \vec{r}} = 1$. This is accomplished only by selecting those band index that lays at the center of the reciprocal lattice (a point normally called Γ).

2.7 The importance of Spin Orbit Coupling in Transition Metal Dichalcogenides

The energy levels of atomic electrons are affected by the interaction between the electron spin magnetic moment and the orbital angular momentum of the electron. It can be visualized as a magnetic field caused by the electron's orbital motion interacting with the spin magnetic moment. This effective magnetic field can be expressed in terms of the electron orbital angular momentum. The interaction energy is that of a magnetic dipole in a magnetic field.

The splitting of atomic spectral lines by the application of an external magnetic field, is called the Zeeman effect. The spin-orbit interaction is also a magnetic interaction, but with the magnetic field generated by the orbital motion of an electron within the atom itself. It has been described as an "internal Zeeman effect". The standard example is the hydrogen fine structure.

The SOC splitting can be calculated from:

Figure 2.4: DFT band structure of the four compounds (a) MoS_2, (b) WS_2 , (c) $MoSe_2$ and (d) WSe_2. Black circles show the results when the SOC on all the atoms are included. Red (blue) lines correspond to the removal of the SOC on the chalcogen (transition metal) atoms[56] [2]

$$E_{so} = \int \Psi^* H_{SO} \Psi d\tau = \frac{Z}{2\alpha^2} \int \Psi^* \frac{\hat{L}\hat{S}}{r^3} \Psi d\tau$$

where Z is the effective atomic number and $\alpha = 137.037$ is the fine structure constant. Once we have integrated for the specific orbital's wavefunction we obtain a general law:

$$E_{so} \approx \frac{Z^4}{2\alpha^2 n^3}$$

where n here is the principal quantum number. We can see from the equation above that the magnitude of the SOC depends on the fourth power of the atomic number. So the heavier the atoms involved in the bonding the stronger the SOC splitting. This has direct consequences in the splitting of the bands in our calculation as we will see later. [57]

The Spin Orbit Coupling (SOC) in the case of the MX_2 is expected to be significantly driven not

only by the d-orbitals of the transition metal M, but also by the p orbitals of the chalcogen X atoms. In fact the splitting of the bands at the K-point is mainly driven by the SOC of the transition metal. Looking at Figure 2.4 we can clearly see the importance of heavier atoms like selenium instead of sulphur and as expected it is observed that a relevant contribution to the SOC splitting comes from the Se atom. This can be seen by a noticeable splitting of the blue lines in Figure 2.4(c) and (d) (for which the SOC due to the metal M has been switched off) which is governed by the SO interaction of the Se atoms[56].

Since we would rather prefer an electrically addressable qubit one key ingredient to look for is the amount of SOC, that can unlock the possibility of addressing electrically the qubit instead of addressing them optically (that is quite difficult to be miniaturized).

2.8   What is $\triangle$SCF

How can we describe excited electronic states of 2D materials? There are a plethora of methods such as Time-Dependent DFT (TDDFT), Green's Function (GW) plus Bethe-Salpeter equation (BSE), but they are really expensive types of calculations to implement. Alternatively we can rely on the ΔSCF methods[58] that are more suitable for a high-throughput screening. The ΔSCF approximation is a density-functional method resembling standard DFT where, in some cases, one or more electrons are placed in higher lying Kohn-Sham states instead of placing all electrons in the lowest possible orbitals as one does when calculating the ground-state energy within standard DFT. It is also possible to remove or add electrons in different states.

In the ΔSCF scheme the positions of the electrons are controlled by assigning the occupation of the Kohn-Sham KS states as the system reaches self-consistency. The ΔSCF scheme has for a long time been justified in cases, where the excited state corresponds to the lowest state of a given symmetry. The scheme has, however, often been applied to more general cases. More recently, Goerling [59] extended the KS formalism to include excited states, such that ΔSCF gets a formal justification in the general case, although a special unknown orbital-dependent exchange-correlation potential should be used for the excited states. In practical implementations standard exchange-correlation potentials from ground-state DFT are typically used[60].

The ΔSCF standard method usually results in a mixture of Singlet and Triplet excited states that prevent us from finding the real energy transition between the ground state and the excited states. This is a problem because we need the real energy of the Singlet excited states to compute the direct transition, not a mixture of Triplet and Singlet.

Frank I., et. al. [61] devised a method to decouple the mixed states and recover the energies of the Singlet and Triplet excited states from them. This process works thanks to spin symmetry, thus a minimum of two determinants is necessary for the description of the wave function of non-

---

[2]Reprinted with permission from ref. [56]
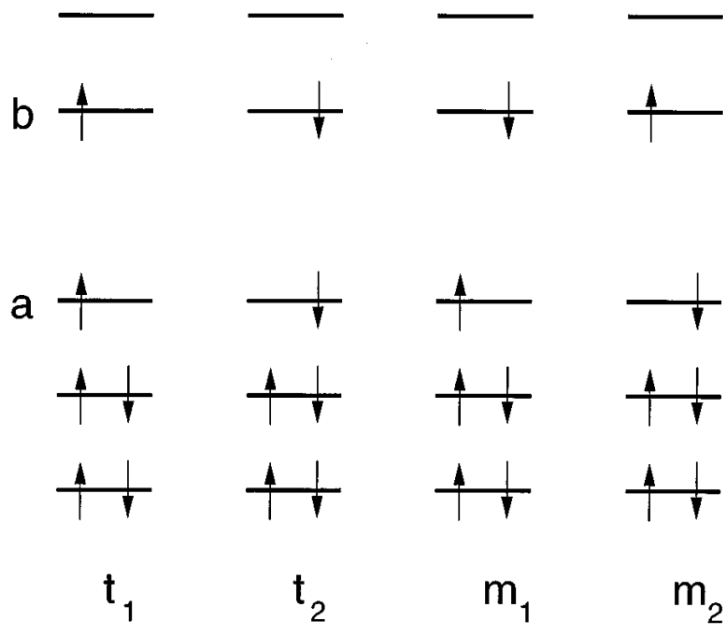
Figure 2.5: Four different states Kohn-Sham electronic configurations representing triplet states t_i and mixed states m_i

degenerate excited singlet states of a closed-shell system. Here we will discuss the construction of such a spin-adapted function and the corresponding energy expression that has to be minimized. Considering a $2n$ system of electrons in a n doubly occupied orbitals it is assumed that the spatial parts of the wavefunctions for spin-up (α) and spin-down (β) are the same, i.e. the authors assume a spin-restricted calculation. If a single electron is transferred from the highest occupied orbital a to the lowest unoccupied orbital b, four different determinants can be formed in accordance with the Pauli principle like in Figure 2.5.

Two of these determinants are degenerate with an expectation value of the square of the total spin angular momentum of $\langle \hat{S}^2 \rangle = S(S+1) = 2$. These triplet functions are denoted by t_1 and t_2 as in Figure 2.5. In general the other two states are not eigenfunctions of $\hat{S}^2$ and they contain a mixture of $\langle \hat{S}^2 \rangle = 0$ and $\langle \hat{S}^2 \rangle = 2$. These states are denoted as m_1 and m_2.
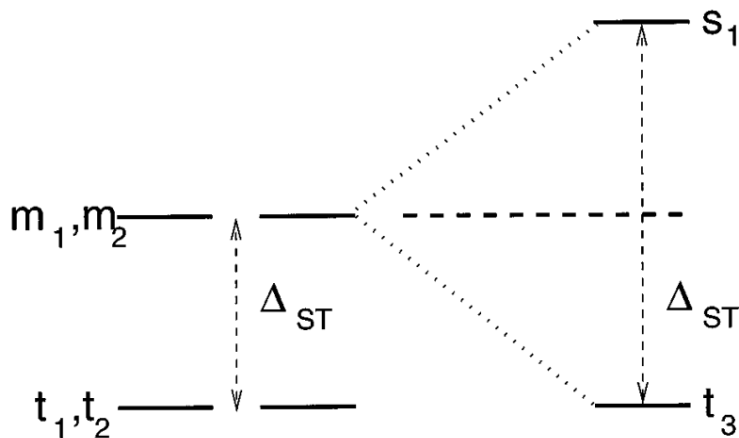
Figure 2.6: Energy diagram depicting the decoupling of the mixed states.

Due to the Pauli repulsion, the mixed state m_i terms are higher in energy than the triplet state t_i terms. This is shown in the energy diagram in Figure 2.6.

Since the m_i states are the barycenter of the two s_1 and t_3, like in Figure 2.6, the energy of the

32

singlet state can be calculated from the energies of the m_i and t_i states via the formula:

$$E(s) = 2E(m) - E(t) \qquad (2.37)$$

where with m we denote the m_1 or m_2 state, with t the t_1 or t_2 state and s we denote the s_1 or s_2 state. In our case to calculate $E(m)$ and $E(t)$ we used DFT theory.

2.8.1   Note on ΔSCF with SOC

In the work of Malis, et al.[62] they assess that the ΔSCF method separately optimizes each excited electronic state, constructing SOC terms or other observables which couple pairs of distinct excited electronic states, e.g. excited singlet or triplet states, and this becomes problematic due to the nonorthogonality between different excited electronic states. Since different sets of molecular orbitals (MOs) are used for each electronic state which are not mutually orthogonal, hereby introducing nonphysical properties. Therefore wave functions are single Slater determinants that directly approximate the wave functions associated with each electronic state density, even though the latter, when made of fractional occupation numbers, cannot be derived from a single determinant. Thus, in order to have a mapping between excited electron density and a single Slater determinant, the procedure is limited to excited electronic states with a dominant single reference character. In other words, such excited electronic states can be described by a single Slater determinant composed of the Kohn-Sham (KS) orbitals, where the square of the determinant gives the corresponding excited electronic state density, like:

$$n^e(\vec{r}) = |\phi_1 \phi_2 \cdots \phi_n|^2 \qquad (2.38)$$

where ϕ_i are mono-electronic wavefunctions of the i-th electron. The excited electronic state Slater determinant is not orthogonal to any other electronic state but can be expanded into a linear combination of Slater determinants composed of KS orbitals of another electronic state, for example, the ground electronic state:

$$\Psi(1, 2, \ldots, N) = \phi_1(1)\phi_2(2) \cdots \phi_N(N) - \phi_1(2)\phi_2(1) \cdots \phi_N(N) + \ldots \qquad (2.39)$$

where in this case we have a spin orbital written as $\phi_j(k) = \varphi(j) \cdot s(k)$, in which φ and s are the spatial and spin part respectively.

Thus the single determinant states are generally more complicated than the one present in a classical ΔSCF due to the presence of the SOC. This leads to an $\hat{H}_{SOC}$ that has the form:

$$
\begin{array}{cccc}
& S & T(1) & T(0) & T(-1) \\
\begin{array}{c} S \\ T(1) \\ T(0) \\ T(-1) \end{array} &
\left(\begin{array}{cccc}
0 & ib+c & ia & ib+c \\
-ib-c & 0 & -id-ie & 0 \\
-ia & id-e & 0 & id-e \\
-ib+c & 0 & -id-e & 0
\end{array}\right)
\end{array}
$$

that is non diagonal and thus we cannot use the strategy of the barycenter as in the previous paragraph. In fact it is very difficult to recover the energies of the eigenstates since the states of the triplets are all mixing with each other. The letters a, b, c, d and e are terms arising from the expectation value of the operator $\hat{H}_{SOC}$, thus they represents energies[62].

2.9   Formation energy of defects

The formation energy E^f of a defect is defined as the energy difference between the investigated system and the components in their reference states. This is analogous to the formation energy of a bulk material, but for charged defects it is less clear how to choose the reference states. Usually a charged system with finite size supercell technique suffers from artificial electrostatic interaction between the periodic defect images and background charge. Therefore, correction scheme is needed to remove this interaction from both the total energy calculation and Kohn-Sham (KS) defect levels. The relative stability of charged defect could be evaluated by the formation energy. In the case where a carbon atom substitute a sulphur one we have[63]:

$$
E^f = E_d - E_{bulk} - \sum_i n_i \mu_i + E_{corr} \tag{2.40}
$$

where E_d is the total energy of the system with defect and E_{bulk} is the total energy of the pristine system without defect. Then $n_i \mu_i$ is the reference energy of n_i added atoms of element i at chemical potential μ_i. E_{corr} is a sum of relevant correctional terms. These could be calculated through supercell size scaling method and Freysoldt-Neugebauer-Van der Walle (FNV) correction as mentioned in their paper[64]. The details and the execution of such method is beyond the scope of this thesis and we will approximate the term of the correction as null. To check the validity of our assumption we should run some tests to see effectively that is a reasonable approximation.

Results

In this chapter we will discuss the results obtained using the suite Quantum Espresso *(QE)[65][66][40] on which we run* $ab\text{-}initio$ *calculations at the level of DFT. We studied two peculiar TMDs, i.e.* MoS_2 *and* WS_2 *with a neutral carbon defect inside them. We chose those two materials because they are promising quantum materials for quantum computing.*

In order to reduce the computational cost but maintaining an overall good accuracy we chose DFT at PBE level as standard for all the materials. In the literature there are proposals for the excited state calculations, of these materials, useful for the characterization of such states that can in principle be used as qubits[39]. However the theoretical framework used in these researches are GWA *and* BSE *that can return the expected properties with high accuracy but also at a high computational cost. These are not suitable for a high-throughput screening of different defects because there needs to be a good compromise between the resources used and the accuracy needed. Thus we want to explore the properties of these defected* $2D$ *materials with a lower computational cost but with a good accuracy overall. Therefore for the calculation of the excited states in the defect we chose a simple but effective strategy, the* ΔSCF *method, which is gaining popularity recently[39][58][67][68] that returns the excitation energies at the cost of a normal* SCF *(Self Consistent Field) calculations.*

In this chapter we will focus on the computational results for each materials. At first we analyze the properties of WS_2 *and compare the results of the calculations with what found in literature, analyzing the different convergence of parameters and the results for the* ΔSCF *method and the formation energies of the defects. Then we will focus on a the other material,* MoS_2, *looking at first at its properties without defects and then with a defect inside a supercell. Finally we discuss the differences and the similarities of these two materials comparing with what we found in the literature.*

3.1 Determining the computational setup

This section summaries different tests that has to be done in order to have good and reliable results out of our calculations. We have chosen different tests each of them will be in a dedicated section, starting with the WS_2 since we can compare it with the literature and then passing to MoS_2. The tests that have been performed were:

- Convergence of energy cut-off

- Convergence of lattice parameter

- Convergence of cell vacuum

- Convergence over K-points for the total energy

- Convergence of supercell size

All the inputs needed to run such tests is reported in Appendix C. In our particular case the two materials, namely WS_2 and MoS_2, share a very similar valence electrons structure, hence the difference in energies calculated in the tests would result very similar to each other. For this reason many of the convergence tests were done only for one material, MoS_2, and the parameters were applied to the WS_2. The only parameter that had to be recalculated was the convergence of the lattice parameter a, shown in Figure 3.1, because in contrast with the other parameters that depend mainly on differences of the total energy of the system, the lattice parameter changes with the chemical nature of the atoms in the unit cell.
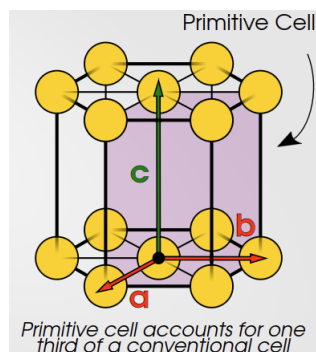
Figure 3.1: Conceptual image of a primitive cell containing the unit cell with lattice parameters a, b and c

As we can see in the Figure 3.1 there is an hexagonal type of lattice but our unit cell will be the violet filled one with the parameters a and b being equal. We will use this unit cell as a reference for our calculation in this section because it's the smallest cell containing all the symmetry operations of the crystal, this is also known as Wigner-Seitz cell. Both the WS_2 and MoS_2 share the same unit cell structure as depicted above.

3.2   Investigation on Tungsten Disulfide (WS$_2$)

3.2.1   Without carbon defect

Convergence of lattice parameters
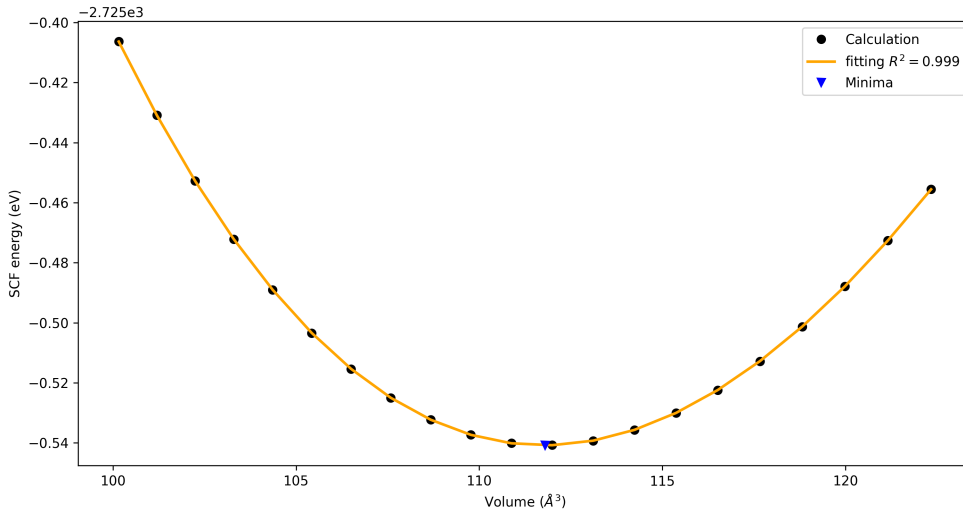
Figure 3.2: Murnaghan fit to retrieve the lattice parameter a from the minima of the total volume.

The first test we conducted was to optimize the cell parameters a (like in Figure 3.1) for both the systems in this thesis relaxing first the coordinates of all three atoms in the unit cell, then increasing it by 0.05 Bohr and relaxing again recording at each step the total energy of the relaxed system. Since the parameter c (the height of the cell like in Figure 3.1) is kept constant during this procedure what affects the volume is just the parameter a. To retrieve the optimal parameter we have to convert it in volume, optimize the curve (find the minima) and then convert back to the value a in Bohr. Due to an integer overflow error (a condition that occurs when an integer calculation produces a result that is greater than what a given register can store or represent) with the optimizer we used a different unit, namely Angstrom, for the volume to keep the number small enough. The formula with which we had to fit the data was the Birch–Murnaghan[69][70]:

$$E(V) = E_0 + \frac{9B_0V_0}{16}\left\{\left[\left(\frac{V}{V_0}\right)^{2/3} - 1\right]^3 B_0' + \left[\left(\frac{V}{V_0}\right)^{2/3} - 1\right]^2 \left[6 - 4\left(\frac{V}{V_0}\right)^{2/3}\right]\right\}. \quad (3.1)$$

Where $E(V)$ is the internal energy, E_0 is the starting internal energy of the system , V_0 is the reference volume, V is the deformed volume, B_0 is the bulk modulus, and B_0' is the derivative of the bulk modulus with respect to pressure. The results obtained from the fitting, that are the minima of the curve, of the Birch-Murnaghan equation are for the WS$_2$ 3.18 Å. In the Figure 3.2 is represented the fitting where the dots are calculated values and the orange line is the fitting curve. We can see that the minimum, represented by a blue triangle, is the point that minimize the a parameter against

37
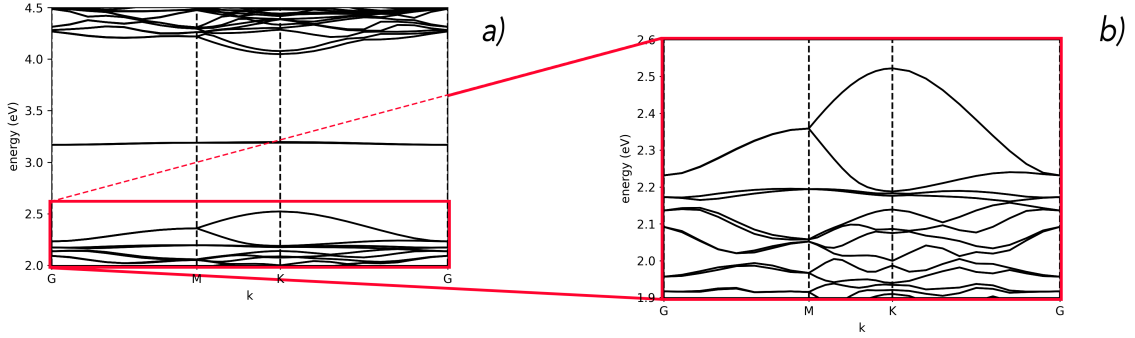
Figure 3.3: Figure representing different bands structure obtained from calculation. In the y-axis there is the energy of bands in eV, in the x-axis the k points of the cell. The image a) and b) are the bands structure of WS$_2$. These images include the carbon defect as a flat energy dispersion inside it.

the total energy. Comparing the experimental result 3.153 Å[71] with our result we obtain an error 0.85% . We can notice that the errors are quite small and thus our data are in agreement with other values of the parameter a find in the literature[71].

3.2.2 With carbon defect

In this section we will discuss the results coming from the calculations run on $5 \times 5 \times 1$ supercells of monolayer WS$_2$ as reference (we chose a $5 \times 5 \times 1$ supercell size based on the results from subsubsection 3.3.2 for the MoS$_2$). Here with defect we mean a carbon atom that substitute a sulphur atom in the supercell. We will comment on the similarities and differences between what is found in the literature and our results, from the band calculations, density of states, projected density of states, isosurfaces, ΔSCF and the convergence of the supercell. In the last one we decided the best supercell based only on the data from MoS$_2$, not repeating it for the WS$_2$ because the two systems are very similar to each other.

Bands structure

The bands in Figure 3.3 are constructed along a k-path, that means that we calculate the bands along selected paths in the Brillouin zone. We can understand better the k-path looking at the Figure 3.4 that show the high symmetry points (Γ , K and M).

On Figure 3.3 b) we see a magnification of the region in the MVB, and as we can see the valence band are splitting (at the K point in the figure that amounts to around 400 meV) due to the large SOC of the materials, in accordance with what is found in the literature[72].
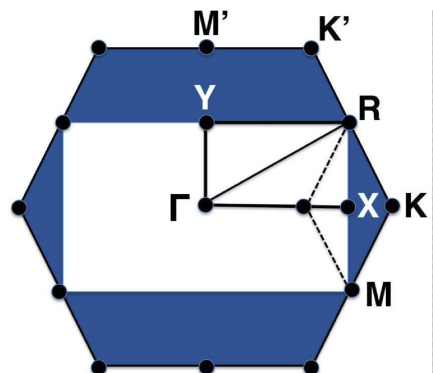
Figure 3.4: The first Brillouin zone with the high-symmetry k-points for MoS$_2$ and WS$_2$

The value of the gap for WS_2 is 1.53 eV in accordance with what found from the theoretical results in the literature of around 1.6 eV[73]. This is somewhat close to experimental values reported of 1.88 eV[74], but as we explained in the previous chapter underestimating the band gap is a well known problem of local and semilocal functionals in DFT.

Density of states
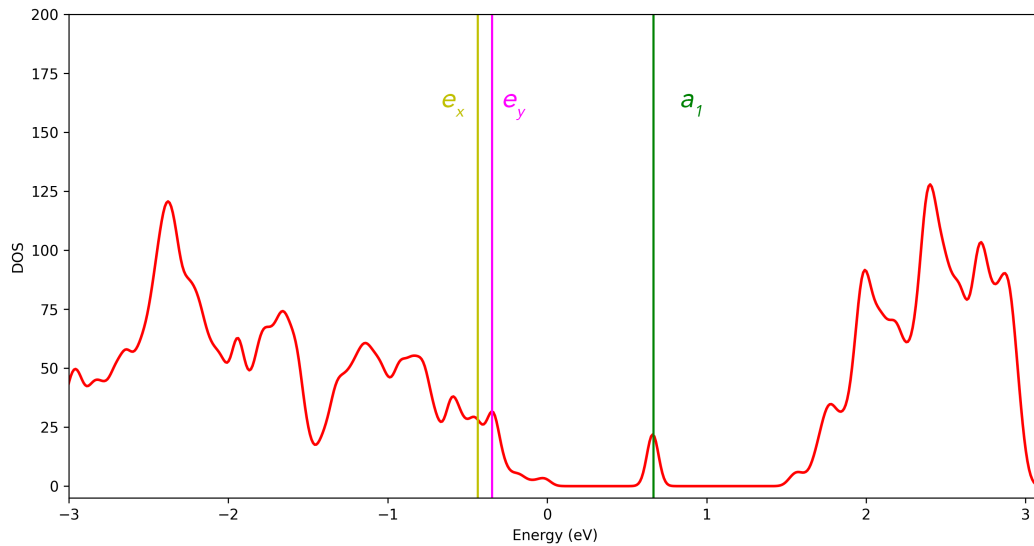
Figure 3.5: DOS for the WS_2 slab, and each important states represented as vertical lines.

From Figure 3.5 we can clearly see the presence of an impurity due to the carbon atom that we inserted in the supercell at around 0.7 eV as we would have expected. Recalling from section 2.5 the shape of the defect in the DOS tells us that the defect is well isolates as a $0D$ quantum dot. In Figure 3.5 are reported the e_x, e_y and a_1 states that we will use later to calculate the direct transitions. In the literature we can find very similar graphs [75] that shows accordance with our results.

Projected density of states
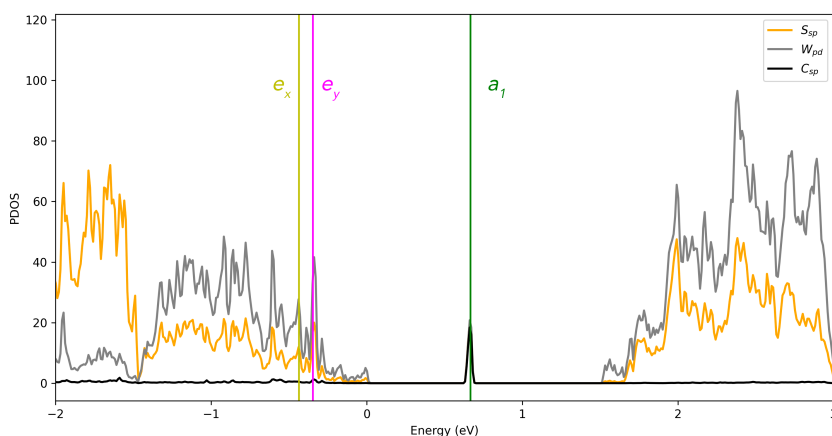
Figure 3.6: Total PDOS of WS_2 with carbon defect and lines representing each state for the carbon defect.
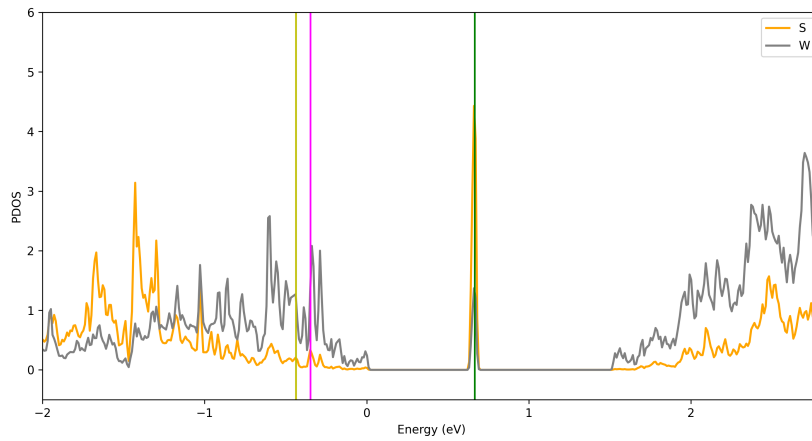
Figure 3.7: PDOS of one atom of S and one atom of W close to the defect in the $5 \times 5 \times 1$ supercell.
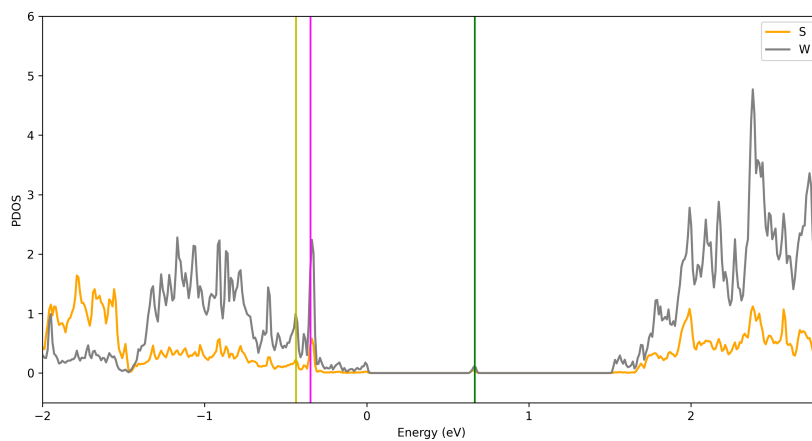
Figure 3.8: PDOS of one atom of S and one atom of W far away from the defect in the $5 \times 5 \times 1$ supercell.

As we can see from Figure 3.6 most of the density of state comes from the contribution of the metal, in particular W, both in the valence and the conductance bands. Moreover the contribution from both the sulphur atoms and the metal contribute significantly to the peak of the defect. A prominent thing to notice is the well isolated nature of the defect inside the bandgap, useful in order to have localized excitations in the material that could be used as a source of qubits.

Moreover in Figure 3.8 we can see a PDOS of W and S taken from atoms far away from the defect and it's peak is drastically diminished from the total PDOS. What is remarkable is comparing the preceding figure with Figure 3.7 in which the PDOS is taken from atoms close to the defect. In this graph we can notice that there is a great component from S in the peak and a little from W. Looking instead in the valence region between -0.5 to -2 eV of the two figure we can see that PDOS for the W reduce from Figure 3.8 to Figure 3.7 meaning that there is non-negligible overlap between the two species next to the defect. The orbitals plotted for those two pictures are the $5d$ for W and $2p$ for S.
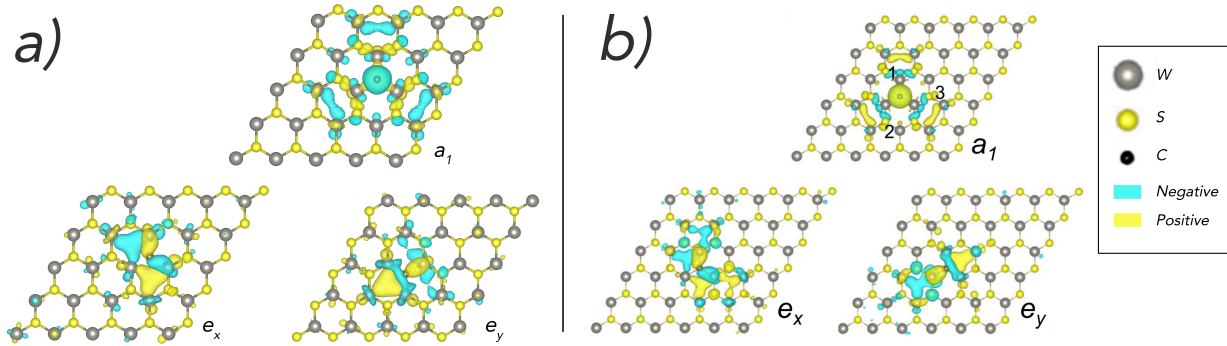
Figure 3.9: Three isosurfaces referring to the distinct orbitals having three different symmetries. All of them are localized orbitals of the carbon atom at the center. a) representing the results from our calculations and b) the one from reference [39]

Analysis of single particle states of the defect

An isosurface is a surface that represents points of a constant value within a volume of space. In this case they represent the amplitude of the Bloch wavefunction on the lattice of atoms. The plots in Figure 3.9 are useful to characterize the different energy levels in Quantum Espresso. This visualization was indeed very helpful in finding those states that were localized on the carbon atom and for which we had to calculate the energy of transition. Being in a C_{3v} symmetry the bands split in energies and the a_1 state is the one that lies within the bandgap. Instead the e_x and e_y states were deeper in the valence bands and are the states from which we made the excitations in the next section.

Excited states of neutral C defect

	WS$_2$			
	E$_{S1}$ (eV)	E$_{T1}$ (eV)	Reference (eV)*	Error (%)
e_y to a_1	1.39	1.01	1.43	3.07
e_x to a_1	1.33	1.04		

Table 3.1: Table representing results from calculation of ΔSCF transitions for WS$_2$ with no SOC accounted. In the rows of the table are reported the direct transition energy from low energy lying states as e_y or e_x to the state a_1. In the columns are instead reported the energies of the Singlet and Triplet states for WS$_2$ as E$_{S1}$ and E$_{T1}$.
*:[39]

We can clearly see a remarkable agreement with the reference data that are calculated with a more expensive functional [39] from Table 3.1 , in terms of computational resources, than the one we used here. The values for the singlets are not the directly collected data from Quantum Espresso, as explained in subsection 2.8.1, the calculation output returns an energy that comes from a mixture of singlet and triplet states[61].

In Table 3.2 we have in the first row the different excitations obtained from the same levels, like in Table 3.1, but with the SOC activated. Previously we could decouple the mixed states using the fact that they are the barycenter of the singlet and the triplet states, but now this strategy no longer holds. Unfortunately we need more insight in what the single wavefunctions actually means before

	WS$_2$	
	EXC1 (eV)	EXC2 (eV)
eya1	1.11	1.11
eya2	1.11	1.12
exa1	1.14	1.14
exa2	1.14	1.15

Table 3.2: Table representing ΔSCF transitions for WS$_2$ with SOC. Where EXC1 and EXC2 should correspond to the Singlet and Triplet transitions respectively, but they are not as explained in subsection 2.8.1. In the rows are reported the transition in SOC picture where the final state (a_1) splits and we have two transitions from e_y, namely eya1 and eya2, and from e_x, namely exa1 and exa2.

drawing any conclusion on the nature of the excited states, as explained in subsection 2.8.1.

Energy of formation of C defect

The formation energies for the WS$_2$ with a carbon defect can be represented as:

$$WS_2 + CH_4 \longrightarrow WS_2@C + H_2S + H_2$$

and the corresponding formation energy value turned out to be 445 kJ/mol from our calculations. What we notice from this value is that we have an endothermic type of reaction prediction. All the values for each species calculated to arrive at the energy of formation can be found in Appendix A.

Another possible reaction to take into account in order to calculate the energy of formation of the carbon defect can be:

$$WS_2 + C \longrightarrow WS_2@C + S$$
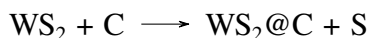
where C is obtained from bulk graphite and S from bulk Sulfur. From the calculation this reaction results in a formation energy of the defect of -211 kJ/mol, in stark contrast with the results obtained in the previous reaction. This is caused by the fact that in the first reaction we are actually breaking and recombining atoms together, that can lead to an increase in the energy of the system, thus making it less favorable. In the second reaction we are idealizing that the only bonds made and broken are relative only to one atom.

3.3 Investigation on Molybdenum Disulfide (MoS$_2$)

3.3.1 Without carbon defect

Convergence of lattice parameters

We conducted the same test to optimize the cell parameters a for MoS$_2$, relaxing first the coordinates of all three atoms in the unit cell, then increasing it by 0.05 Bohr and relaxing again recording at each step the total energy of the relaxed system. Since the parameter c is kept constant during this
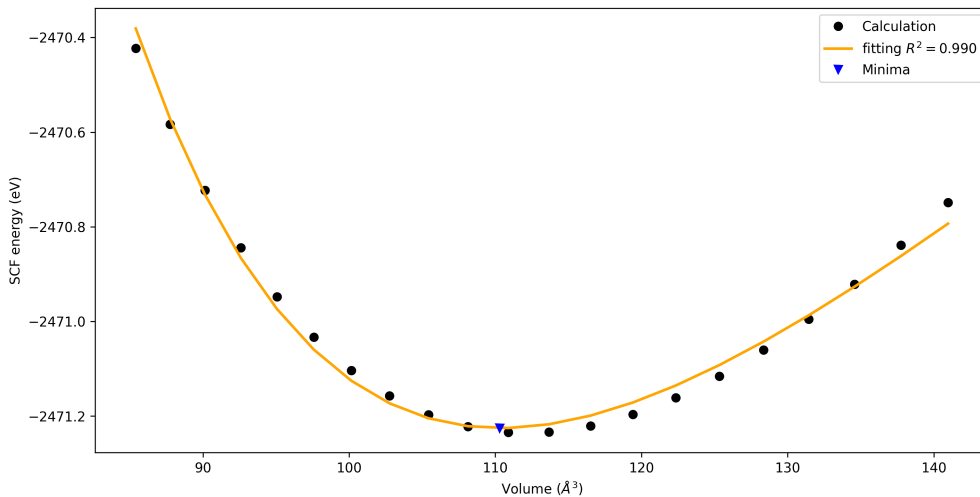
Figure 3.10: Murnaghan fit to retrieve the lattice parameter a from the minima of the total volume.

procedure what affects the volume is just the parameter a as in the case for WS_2. The formula with which we had to fit the data was the Birch–Murnaghan shown in Equation 3.1 [69][70].

The result obtained from the fitting, that is the minima of the curve, of the Birch-Murnaghan equation for the MoS_2 is 3.19 Å. In the Figure 3.10 the dots are calculated values and the orange line is the fitting curve. We can see that the minimum, represented by a blue triangle, is the point that minimize the a parameter against the total energy. Comparing with 3.160 Å[71] respectively we obtain an error of 1.06%. As for the WS_2 we can notice that the error is quite small and thus our data are in agreement with other values of the parameter a find in the literature[71].

The present Table 3.3 show the recap of all the a lattice value for both the substrates:

a (Å)	MoS_2	WS_2
Calculated	3.19	3.18
Experimental*	3.160	3.153

Table 3.3: Relaxed lattice parameters for MoS_2 and WS_2 and experimental lattice parameters. All lattice parameters are given in Å.
*: [71]

Convergence of cell vacuum

To run our calculation we need to be sure that the replicas on the z-axis of the supercell do not interact significantly. In order to prevent interactions we had to use a vacuum layer big enough, that means not too small for the interaction to leak in, but not too big to make the calculation too heavy. To do this test it requires three parameters to take into account: SCF energy, bandgap value and the c/a ratio .We chose to compare the energy and the bandgap (right and left y-axis of Figure 3.11) to be sure that both of them are well converged. So we fixed the a value and then varied the height of the cell to modify the vacuum inside the cell. Obviously every single time the supercell is scaled the parameter c/a ratio has to be scaled to keep the same height. From Figure 3.11 we chose a
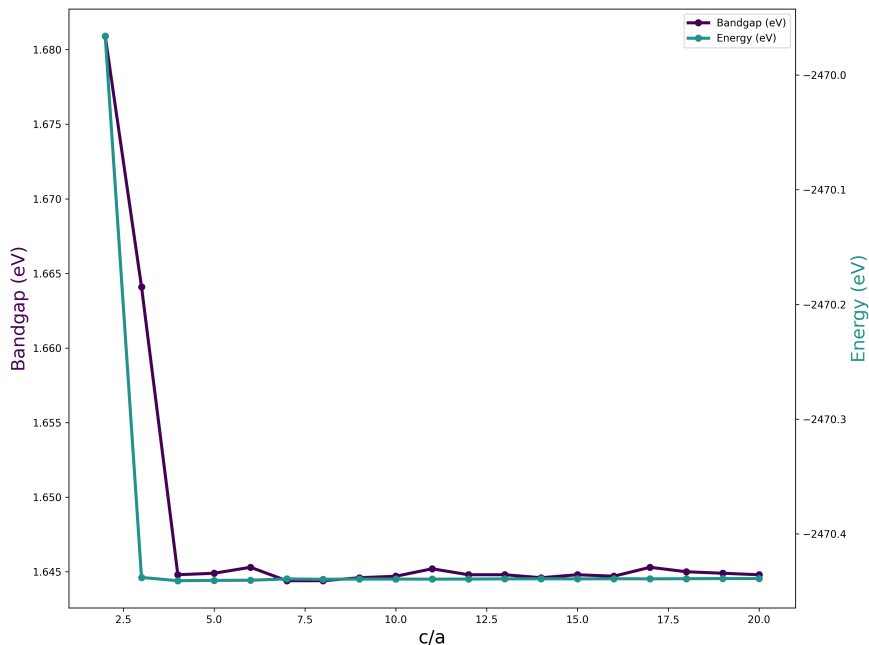
Figure 3.11: The axis on the right and left stand for the total energy from the SCF calculations and for the bandgap in eV. On the x-axis is reported the ratio c/a that represents how many times the height of the cell c is a multiple of the lattice parameter a.

conservative value of 4, that translates to roughly 12 Å of height c, because this value described better the bandgap of the system in consideration, meaning that the bandgap value has converged with respect to the c/a value.

Convergence over k-points

As we can see from Figure 3.12 the value of k-points for the planar grid $n \times n \times 1$ (in the simplest case, a k-point grid is specified by a product of three integer numbers in the three spatial dimensions, e.g., a $10 \times 10 \times 10$ grid. This is a way to discretize our calculation in the reciprocal space) was optimized following the trend of the energy against the number n. We see that together with the bandgap parameter the best value of n was 6. This means that we can recover a good quality of the calculation using a grid that is not too dense, hence we can use less k-points to have a good result and at a lower computational cost. Other sources use values super-cell size up to $12 \times 12 \times 1$[76].
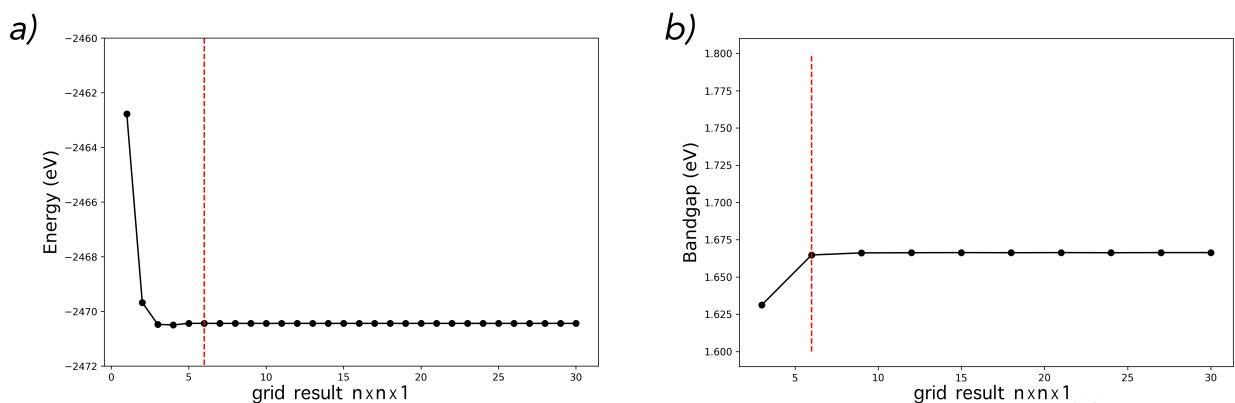
Figure 3.12: In panel a) we can see a plot of variation of the number K-points against the total energy of the system. In panel b) the number of K-points are varied following the change in the bandgap energy. The red dotted line shows the threshold at the optimal value 6.

Convergence of energy cutoff
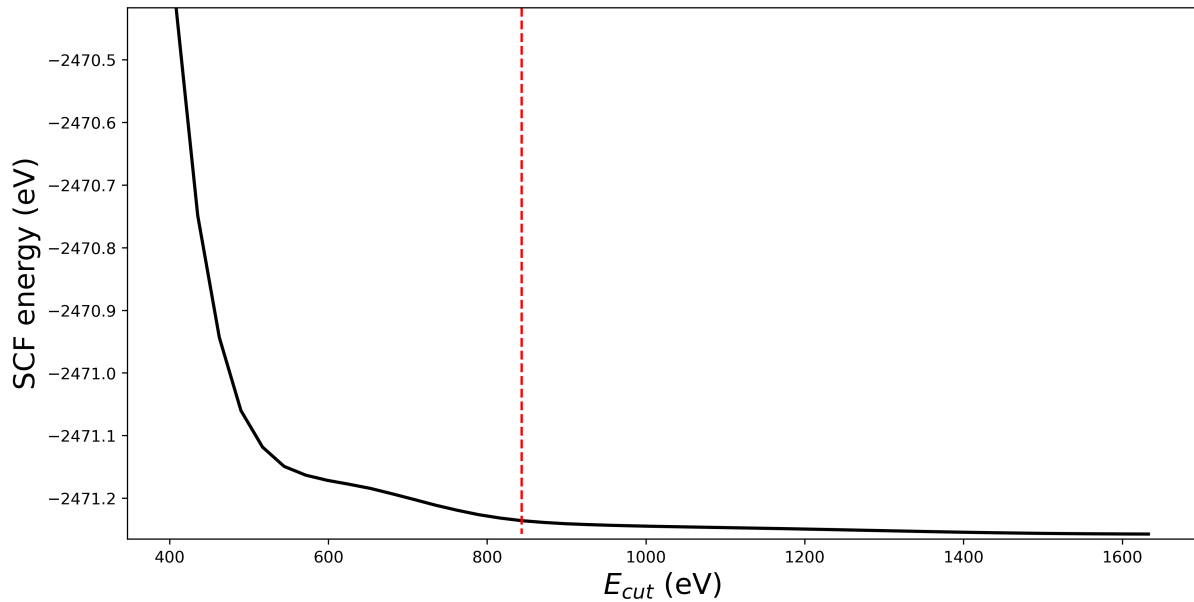
Figure 3.13: In this graph it is reported the energy of the SCF against the cutoff of the energy for the plane waves. The red line indicates the optimal value chosen for our calculation in the SOC regime.

The convergence of the energy cut-off (E_{cut}) limits the number of plane waves used in the calculations. In the case of the plane-wave representation, the energy cut-off is the kinetic energy of the plane wave with highest wave vector like we have seen in Section subsection 2.3.2. The higher this cut-off is, the more waves will be used to represent the orbitals, the more accurate the description of the system will be. With $E_{cut} \longrightarrow \infty$ we recover the exact solution in the usual atomic basis set. Thus the best value chosen for the cut-off was 843.2 eV because it was the first value with a significant gap of energy from the preceding.

3.3.2   With carbon defect
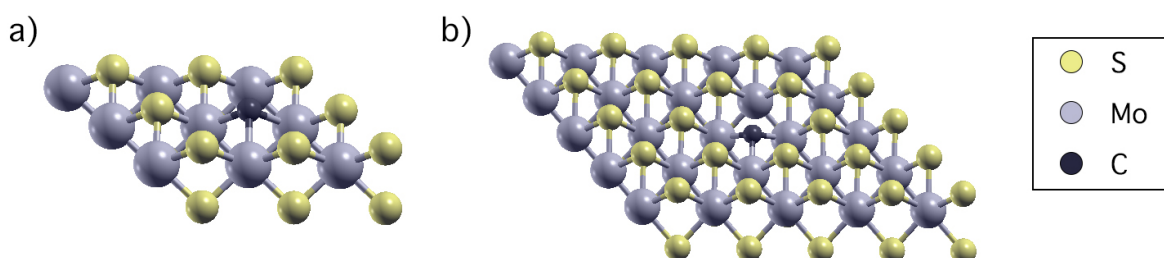
Figure 3.14: Two representations of MoS$_2$ with carbon defect in it. In panel a) we have a representation of a $3 \times 3 \times 1$ supercell. In panel b) we have a representation of a $5 \times 5 \times 1$ monolayer supercell.

As above-mentioned we decided to use a supercell $5 \times 5 \times 1$, as reported in Figure 3.14 panel b), based on the following results.

Convergence of supercell size
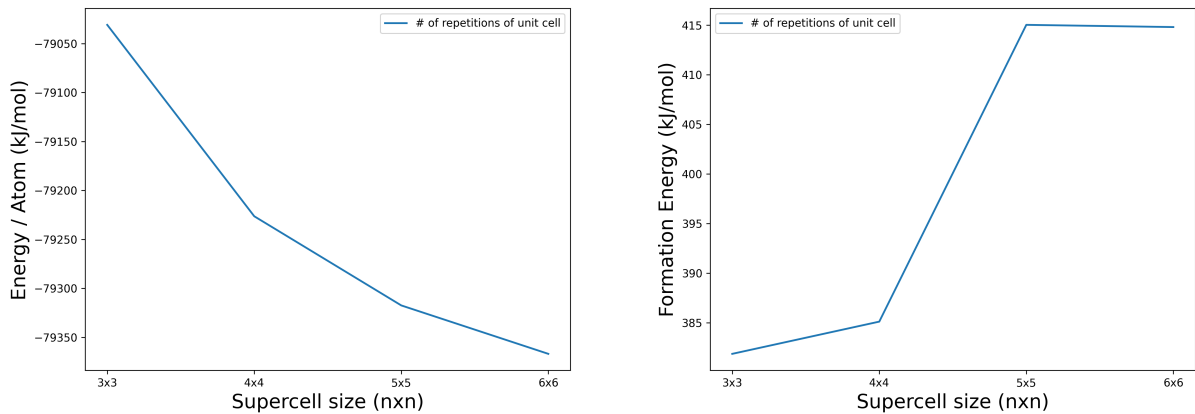
Figure 3.15: The graph depicts the energy over atom of a supercell against the number of copies of the unit cell. Panel a): total energy per atom as a function of the supercell size for a MoS$_2$ layer including a neutral C defect. Panel b): we see an increase of the formation energy increasing the number of supercells.

Within the Periodic Boundary Conditions (PBC) approach we need to ensure the interactions between the replicas to be minimal. In fact to study appropriately the system with a neutral carbon atom in it we have to evaluate which is the best cell dimension that minimizes such interactions. Since we are dealing with a monolayer we start by taking the unit cell and repeat it multiple times in the x and y dimensions obtaining a supercell in which we insert a carbon defect. The notation that we will use is $n_x \times n_y$ where n_i stands for the number of times the unit cell is repeated along the $i - th$ direction. We have thus created four different supercells from 3×3 to 6×6 at step of one and calculated their total energy, dividing it by the number of atoms. In this way we can see that the interaction with the copies in the PBC, that are replicas of the system along each direction in space, is smoothly decreasing as we can see in the Figure 3.15 panel a). We could have used a larger supercell, such as 9×9, to see the limit, but the constrain on our computational resources imposed just smaller supercell. Moreover even in literature[39][71] we can find examples of calculation done with small supercell of size 4×4. We chose, for constrains imposed by the resources available, a supercell of size 5×5, the relaxed coordinates of such surpercells can be found at Appendix B. The approach just used, inspired by the literature, is however questionable in the sense that the energy per atom could change by enlarging the cell even if the interaction between defects has become negligible. In order to assess more thoroughly that the optimal value was indeed a 5×5 we have done the same calculation using the formation energy, as in figure Figure 3.15 panel b). In this case we have an agreement between the two methods. We can see that the formation energy starts to stabilize at the supercell 5×5. Moreover the change of the formation energy is towards increasing values, meaning that the interaction between the defects are stabilizing. When we studied the optimal value for the grid size we obtained a value of 6. Since we are expanding the number of points to be computed in real space, we can reduce the number of K-points by the amount of the expansion of the supercell,

46

e.g. if we have a unit cell (1×1) calculated with a grid of $6 \times 6 \times 1$ and then we pass at a supercell 3×3 we can divide by 3 the number of the grid points, yelding a grid of only $2 \times 2 \times 1$[77].

Bands structure
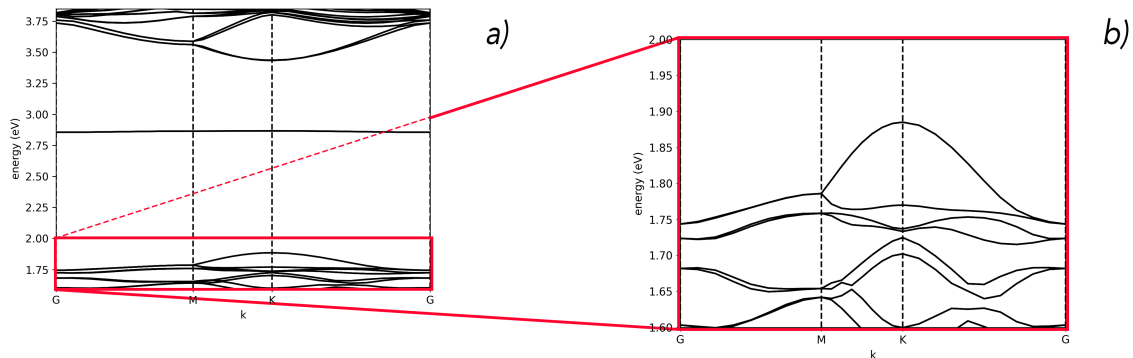
Figure 3.16: Figure representing different bands structure obtained from calculation. In the y-axis there is the energy of bands in eV, in the x-axis the k points of the cell. The image a) and b) are the bands structure of MoS_2. In a) we can see the whole frontiers band structure of the material, while in b) we can see the magnification of the valence band and how the SOC affects it.

For the MoS_2 we chose the same k-path mentioned in the subsubsection 3.2.2 to have comparable plots between what we have calculated and what is found in the literature. As we noticed with the WS_2 there's a splitting of the band due to the large SOC. In the case of MoS_2 this amounts to 115 meV as in Figure 3.16 b), this results match what is found in literature[72].

In literature we found as reference value, for DFT at level of PBE, of around 1.6 eV[73]. The value of the gap from our calculations for MoS_2 is 1.56 eV with an error of 2.5%. Moreover for the MoS_2 the bandgap energy is in accordance with the experimental value reported of 1.88 eV[74].

Density of states
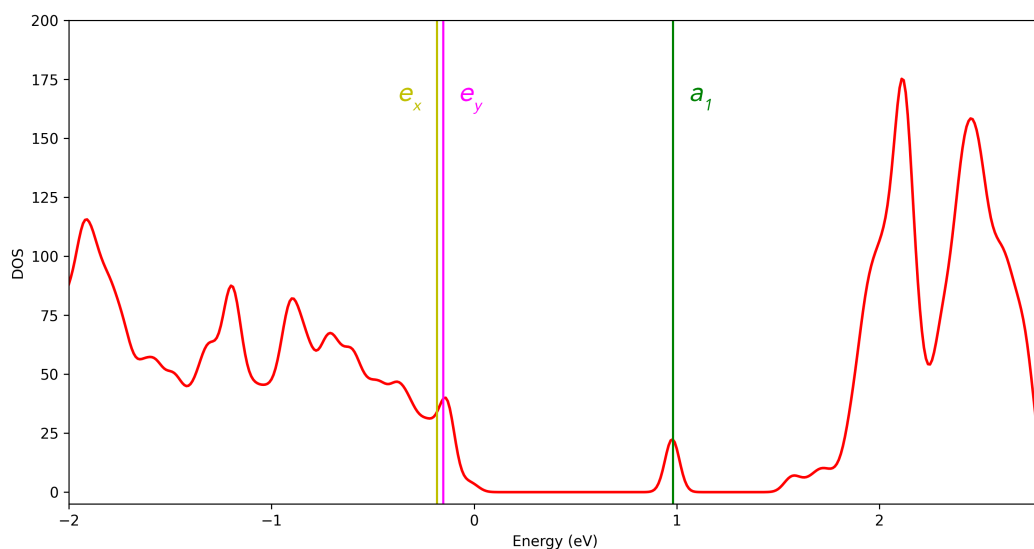
Figure 3.17: Figure representing the DOS for MoS_2. Each line correspond to the states in carbon defect.

47

The density of states gives the number of allowed electron (or hole) states per unit volume at a given energy. From the Figure 3.17 we can see for the MoS_2 a peak at around 1 eV confirming the presence of our defect supercells. In the literature we can find very similar graphs as shown here[75].

Projected density of states

In general the Projected Density Of States (PDOS) is the projection of a particular orbital of a particular atom on the density of states. So, if we sum over all the projections, we will have the total density of state, or simple, the DOS. These are useful tools to obtain information and insight relevant to important applications.
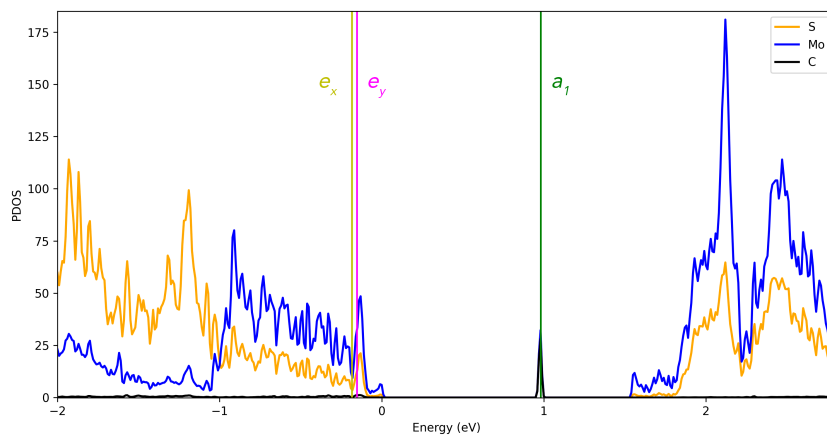
Figure 3.18: PDOS of MoS_2 with carbon defect and different lines for each state of the localized carbon defect.
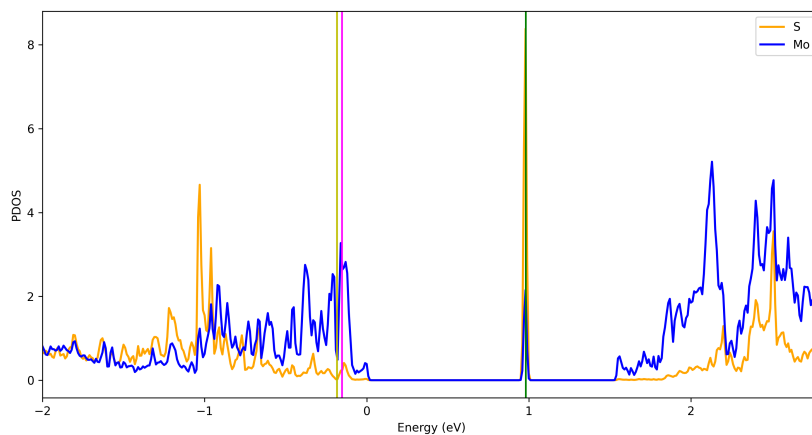
Figure 3.19: PDOS of one atom of S and one atom of Mo close to the defect in the $5 \times 5 \times 1$ supercell.

In Figure 3.18 we can find the same contribution, as in the WS_2, with a slight more accented peak in the region of 2 eV for the MoS_2. Even in this case we find the same pattern as in WS_2, so passing from far way, Figure 3.20, to close to the defect, Figure 3.19, we can find that there's a better overlap between Mo and S in the region between $[-2, -0.5]$ eV. There's an accented peak at -1 eV in this case that is not present in the PDOS of single atoms in the WS_2 system.
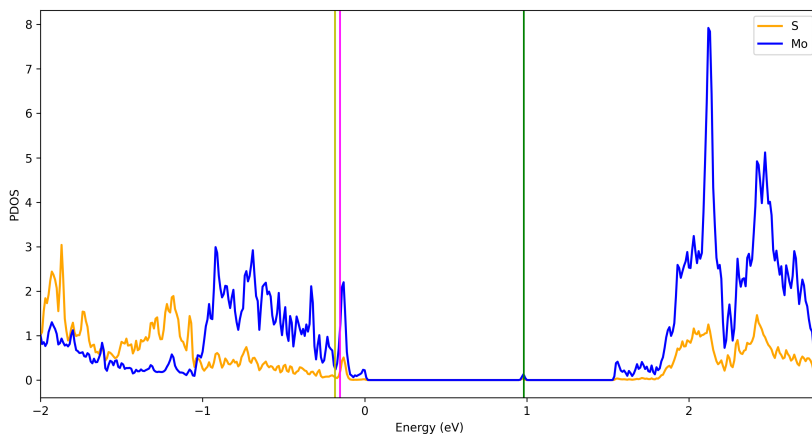
Figure 3.20: PDOS of one atom of S and one atom of Mo far away from the defect in the $5 \times 5 \times 1$ supercell.

Energy of formation of C defect

We used a similar reaction environment for the formation of the defect as in the case for WS_2 and is represented by:

$$MoS_2 + CH_4 \longrightarrow MoS_2@C + H_2S + H_2$$

What we notice from the value returned from the calculation, of around 434 kJ/mol, is that we have an endothermic type of reaction as in the case for the WS_2. And as we mentioned for the last one the intervention of an external factor is a must (like a presence of defect or an STM tip that controls where the defect should go)[73]. All the values for each species calculated to arrive at the energy of formation can be found in Appendix A.

As we have seen in case for the WS_2 we can have another possible energy of formation:

$$MoS_2 + C \longrightarrow MoS_2@C + S$$
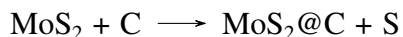
and from the calculation this reaction results in -222 kJ/mol, as we would have expected in in plain contrast with the reaction above.

Excited states of neutral C defect

	MoS$_2$	
	E_{S1} (eV)	E_{T1} (eV)
e_y to a_1	1.42	1.08
e_x to a_1	1.42	1.10

Table 3.4: Table representing results from calculation of ΔSCF transitions for MoS$_2$ with no SOC.

In the rows of the Table 3.4 are reported the direct transition energies from low energy lying states as e_y or e_x to the state a_1. In the columns are instead reported the energies of the Singlet and Triplet states, for MoS$_2$, respectively as E_{S1} and E_{T1}. In this case there are no reference values to compare our results with, because the MoS$_2$@C was not investigated before.

49

	MoS$_2$	
	EXC1 (eV)	EXC2 (eV)
eya1	1.22	1.23
eya2	1.22	1.23
exa1	1.26	1.27
exa2	1.26	1.27

Table 3.5: Table representing ΔSCF transitions for MoS$_2$ with SOC. Where EXC1 and EXC2 should correspond to the Singlet and Triplet transitions respectively, but they are not as explained in subsection 2.8.1. In the rows are reported the transition in SOC picture where the final state (a_1) splits and we have two transitions from e_y, namely eya1 and eya2, and from e_x, namely exa1 and exa2.

In Table 3.5 we can see in the first row the different excitations done from the same levels as before but with the SOC activated. The problem is the same as for the case with WS$_2$ and a possible rationale is given in the subsection 2.8.1.

3.4 Discussion

The properties for the two defected carbon materials are until this point quite similar. We have seen that the bandgap for the two systems is close to each other and around 1.6 eV in contrast with what is found as experimental value of 1.88 eV[74]. This is mostly due to the level of theory chosen and we have discussed why they differ so much in section 2.4.

Moreover we have the isolated state of the defect in MoS$_2$ differs by 0.3 eV with respect to the corresponding one in WS$_2$. This tell us that there is a non-negligible effect due to the type of substrate in which the defect is inserted.

Finally the two energies of formation for the defect in the two materials does not differ by much, and thus there is no net advantage of choosing one over the other from the thermodynamic point of view.

In conclusion the two materials are quite similar when we compare them. Is thus the defect that hold the keys for a promising quantum material? To answer this question we should compare, like we have done here, different materials but also with different defects in them. This can be done employing an HTS that could enable us to simulate more materials in parallel, select the few that are most promising and refining the calculation with higher level of theory, a work that can be seen as a perspective of this thesis.

Conclusions

The aim of this project was to find the most efficient way to simulate a given TMDcs with carbon as a defect. The defect is a key ingredient in order to space-confined excitation useful for a solid-state qubit. We explained what are the current proposals for new materials to host qubits (Chapter 1) and the advantage and disadvantage of using DFT theory to simulate the properties of materials (Chapter 2). We have seen also how a quantum computer can be built and what are the key features to host manipulable and measurable qubits in it. This leads us to hypothesize new materials to be investigated with a low cost strategy (in terms of computational performance) to recover the important information about the systems taken in consideration, i.e. MoS_2 and WS_2 (Chapter 3). In the last Chapter we have successfully reproduced and optimized previous findings in literature and proposed and studied a new material in comparison. We also stressed how changing the material can have only subtle variations at the level of electronic landscape. We thus need to compare the same material with different types of defect to judge if the characteristics we are seeking resides either in the material or in the defect per se. With our work we aim at expanding this knowledge through a so called high-throughput screening, a method for scientific experimentation and computing especially used in drug discovery and rapidly expanding to the fields of biology, materials science and chemistry. What we expect in the future from this technique is to find, among many possible candidates, the best quantum material. With this we could be able to build a functioning qubit, galvanizing the attention of experimentalists to synthesise what we find the most interesting materials. This would not have been possible without this thesis that lead in this direction and find its roots in looking for the lowest cost possible type of calculations. This was done in order to predict important properties, like the direct transition in a defect using ΔSCF and using all the other diagnostic tools to build credential.

In conclusion this thesis leveraged the knowledge of DFT theory implemented in Quantum Espresso to build a solid starting point for further research and helped myself to really understand what are the key ingredients for a good qubit to be realized. Chemistry and Quantum Computing are very interconnected, the first can help the second finding optimal materials to be used, the second can help the first simulating what Quantum Chemistry cannot do (or otherwise can do but at a very high cost).

Appendix A

Table representing all the reactions energies for each single species to calculate the energy of formation.

MoS_2	SCF (Ry)	kJ/mol	WS_2	SCF (Ry)	kJ/mol
CH_4	-17.18901192		CH_4	-17.18901192	
SH_2	-23.28897961		SH_2	-23.28897961	
H_2	-2.33323174		H_2	-2.33323174	
MoS_2	-4539.48842562		WS_2	-4999.4209720261	
$MoS_2@C$	-4530.72483157		$WS_2@C$	-4990.64891526	
Result	0.33	434	Result	0.34	445

Table A.1: Table reporting the data from which we calculated the energy formation for the defected WS_2 and MoS_2 starting from the reaction find in the literature[73].

Appendix B

B.1 Coordinates of relaxed WS$_2$@C

The following are the relaxed coordinates given in the units citing the *pw.x* manual online this units are defined as : *atomic positions are in crystal coordinates, i.e. in relative coordinates of the primitive lattice vectors as defined either in card CELL_PARAMETERS or via the ibrav + celldm or a,b,c... variables.*

These relaxed coordinates of the defect were obtained all using QE v 6.5 at DFT level of theory with a PBE functional and scalar relativistic ultrasoft pseudopotentials (directly downloadable from the quantum espresso library). The supercell used was a $5 \times 5 \times 1$.

```
ATOMIC_POSITIONS (crystal)
W           0.0664548919      0.1332935974      0.2796114564
W           0.2665730599      0.1339274064      0.2787829971
W           0.4673659625      0.1339319637      0.2787874435
W           0.6668517542      0.1332917928      0.2795939386
W           0.8666703501      0.1333296499      0.2796417478
W           0.0664530163      0.3331562323      0.2796064370
W           0.2658964384      0.3329529529      0.2774182032
W           0.4675662667      0.3351580414      0.2738939301
W           0.6670422193      0.3329577807      0.2774311568
W           0.8667082072      0.3331482458      0.2795939386
W           0.0666183772      0.5332388231      0.2803227715
W           0.2665629987      0.5326430468      0.2787694191
W           0.4675665142      0.5324334858      0.2738835408
W           0.6648419586      0.5324337333      0.2738939301
W           0.8660680363      0.5326340375      0.2787874435
W           0.0663562384      0.7331685286      0.2800923886
W           0.2668277131      0.7331722869      0.2801046344
W           0.4673569532      0.7334370013      0.2787694191
```

W	0.6670470471	0.7341035616	0.2774182032
W	0.8660725936	0.7334269401	0.2787829971
W	0.0666268566	0.9333731434	0.2803062492
W	0.2668314714	0.9336437616	0.2800923886
W	0.4667611769	0.9333816228	0.2803227715
W	0.6668437677	0.9335469837	0.2796064370
W	0.8667064026	0.9335451081	0.2796114564
S	0.1337420097	0.0672853769	0.4032229866
S	0.3339792814	0.0679438331	0.4026248632
S	0.5335703504	0.0673037141	0.4032269688
S	0.7334971645	0.0667472558	0.4032650866
S	0.9332545093	0.0667454907	0.4032723070
S	0.1336764594	0.2668379451	0.4025567949
S	0.3355445838	0.2694618015	0.4001906839
S	0.5338916402	0.2694590038	0.4002044301
S	0.7331666283	0.2668333717	0.4025438168
S	0.9332527442	0.2665028355	0.4032650866
S	0.1337410347	0.4664463306	0.4032255985
S	0.3355617088	0.4661055505	0.4001652026
C	0.5333153199	0.4666846801	0.3458161773
S	0.7305409962	0.4661083598	0.4002044301
S	0.9326962859	0.4664296496	0.4032269688
S	0.1333421340	0.6666800890	0.4036579155
S	0.3339799803	0.6660200197	0.4026408115
S	0.5338944495	0.6644382912	0.4001652026
S	0.7305381985	0.6644554162	0.4001906839
S	0.9320561669	0.6660207186	0.4026248632
S	0.1333484347	0.8666515653	0.4036317428
S	0.3333199110	0.8666578660	0.4036579155
S	0.5335536694	0.8662589653	0.4032255985
S	0.7331620549	0.8663235406	0.4025567949
S	0.9327146231	0.8662579903	0.4032229866
S	0.1327954114	0.0662217547	0.1563897865
S	0.3333230441	0.0666297837	0.1561915834
S	0.5334279044	0.0662191077	0.1563867314
S	0.7333957169	0.0666907954	0.1560754344

S	0.9333092566	0.0666907434	0.1560840331
S	0.1317968742	0.2658968409	0.1551194960
S	0.3311472748	0.2652462453	0.1534046072
S	0.5340947418	0.2652542859	0.1534180040
S	0.7340912174	0.2659087826	0.1551304958
S	0.9333092046	0.2666042831	0.1560754344
S	0.1327784670	0.4665683393	0.1563941185
S	0.3311351315	0.4659071366	0.1533843480
S	0.5333281032	0.4666718968	0.1434554676
S	0.7347457141	0.4659052582	0.1534180040
S	0.9337808923	0.4665720956	0.1563867314
S	0.1333182356	0.6666016705	0.1568549836
S	0.3333075336	0.6666924664	0.1561799790
S	0.5340928634	0.6688648685	0.1533843480
S	0.7347537547	0.6688527252	0.1534046072
S	0.9333702163	0.6666769559	0.1561915834
S	0.1333114364	0.8666885636	0.1568406959
S	0.3333983295	0.8666817644	0.1568549836
S	0.5334316607	0.8672215330	0.1563941185
S	0.7341031591	0.8682031258	0.1551194960
S	0.9337782453	0.8672045886	0.1563897865

End final coordinates

B.2 Coordinates of relaxed MoS$_2$@C

In this section we report the relaxed coordinates of MoS$_2$ with a carbon defect in a 5×5 supercell in the same units crystal as before. The calculation were all run using QE v 6.5 at the level of DFT theory and PBE as functional, moreover we used scalar relativistic ultrasoft pseudopotential for this kind of optimization.

```
ATOMIC_POSITIONS (crystal)
```

Mo	0.0664577351	0.1332363066	0.2520452194
Mo	0.2665560757	0.1338325451	0.2508610672
Mo	0.4672763831	0.1338326206	0.2508611051
Mo	0.6667784167	0.1332363747	0.2520453046
Mo	0.8666666197	0.1333331803	0.2522017314
Mo	0.0664578278	0.3332213373	0.2520453028
Mo	0.2660731335	0.3330364149	0.2495842100
Mo	0.4670170428	0.3340340992	0.2447147315
Mo	0.6669630846	0.3330367154	0.2495841984
Mo	0.8667634253	0.3332213833	0.2520453046
Mo	0.0666478786	0.5332959020	0.2526913262
Mo	0.2665559243	0.5327234417	0.2508613246
Mo	0.4670172777	0.5329825223	0.2447147269
Mo	0.6659657008	0.5329827572	0.2447147315
Mo	0.8661671794	0.5327234169	0.2508611051
Mo	0.0664941145	0.7332470152	0.2524112170
Mo	0.2667527857	0.7332470143	0.2524112441
Mo	0.4672763583	0.7334438757	0.2508613246
Mo	0.6669633851	0.7339266665	0.2495842100
Mo	0.8661672549	0.7334437243	0.2508610672
Mo	0.0666478907	0.9333519093	0.2526912606
Mo	0.2667527848	0.9335056855	0.2524112170
Mo	0.4667038980	0.9333519214	0.2526913262
Mo	0.6667784627	0.9335419722	0.2520453028
Mo	0.8667634934	0.9335420649	0.2520452194
S	0.1339119742	0.0673769539	0.3748081833
S	0.3339627600	0.0679256103	0.3740862352
S	0.5334649591	0.0673770616	0.3748082587
S	0.7333650327	0.0666825655	0.3749857611

S	0.9333173333	0.0666824667	0.3749857151
S	0.1339552434	0.2669774906	0.3740445385
S	0.3359743923	0.2696429577	0.3712798228
S	0.5336685199	0.2696430524	0.3712799382
S	0.7330221572	0.2669776428	0.3740445970
S	0.9333172345	0.2666347673	0.3749857611
S	0.1339119135	0.4665349865	0.3748082520
S	0.3359740902	0.4663310901	0.3712800763
C	0.5333333393	0.4666664607	0.3118369735
S	0.7303567476	0.4663312801	0.3712799382
S	0.9326227384	0.4665348409	0.3748082587
S	0.1333424334	0.6666852368	0.3752931891
S	0.3339627204	0.6660370796	0.3740862564
S	0.5336687099	0.6640257098	0.3712800763
S	0.7303568423	0.6640254077	0.3712798228
S	0.9320741897	0.6660370400	0.3740862352
S	0.1333425788	0.8666572212	0.3752931461
S	0.3333145632	0.8666573666	0.3752931891
S	0.5334648135	0.8660878865	0.3748082520
S	0.7330223094	0.8660445566	0.3740445385
S	0.9326228461	0.8660878258	0.3748081833
S	0.1326224522	0.0660544499	0.1294558127
S	0.3332134275	0.0664268871	0.1291302968
S	0.5334319097	0.0660544340	0.1294559265
S	0.7334498354	0.0667250199	0.1293203778
S	0.9332748290	0.0667249710	0.1293203261
S	0.1317255130	0.2658626968	0.1284024347
S	0.3306985363	0.2649197014	0.1258550149
S	0.5342211585	0.2649198051	0.1258549505
S	0.7341370773	0.2658627227	0.1284024001
S	0.9332747801	0.2665499646	0.1293203778
S	0.1326223644	0.4665679927	0.1294560215
S	0.3306982526	0.4657785487	0.1258549545
S	0.5333333483	0.4666664517	0.1164474841
S	0.7350799949	0.4657786415	0.1258549505
S	0.9339453660	0.4665678903	0.1294559265

S	0.1333022976	0.6666048550	0.1298958405
S	0.3332134235	0.6667863765	0.1291306358
S	0.5342212513	0.6693015474	0.1258549545
S	0.7350800986	0.6693012637	0.1258550149
S	0.9335729129	0.6667863725	0.1291302968
S	0.1333023899	0.8666974101	0.1298959162
S	0.3333949450	0.8666975024	0.1298958405
S	0.5334318073	0.8673774356	0.1294560215
S	0.7341371032	0.8682742870	0.1284024347
S	0.9339453501	0.8673773478	0.1294558127

Appendix C

C.1   Main script used for all the calculations

In this section we explain the file structure and how the code works. First of all in Figure C.1 we see the input file written in Bash (Bourne Again SHell) at the root of the folder. This file contains the set of instructions in order to compute all the possible combination of calculations needed to return the results of this thesis. In the *inputs* folder are located the atomic coordinates needed as an input for quantum espresso. In the *outputs* folder are found all the outputs file from a quantum espresso run.
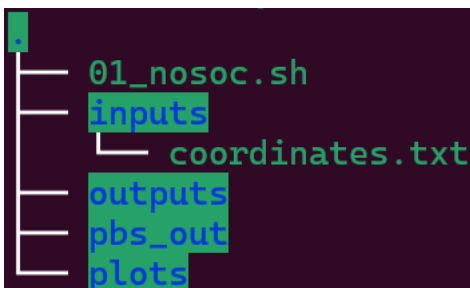
Figure C.1: Tree structure of the folder used to run the calculations and record the results.

The script can execute in parallel (using the Message Passing Interface, MPI) different kind of calculations, from SCF, NSCF, bands, and all the post processing needed to extract the data that we want. In the first section of the code there is a choice to be maid that can be either starting right from the input file *coordinates.txt* for an SCF calculation or choosing a relax calculation and then proceed for all the remaining calculation. We can choose which type of calculation to run with the string *y* or *n*. Each section will generate an input file, fed it to QE and then return an output in the *outputs* folder.

```
#! /bin/bash


#PBS -N ********************
#PBS -o ./pbs_out/
#PBS -e ./pbs_out/
#PBS -q NAME_OF_THE_QUEUE
```

```
#PBS -l nodes=1:ppn=16
#PBS -l walltime=24:00:00
#PBS -W group_list=NAME_OF_THE_GROUP


# Set the name of the folder and move to it
cd /your/path/to/folder
# Modules to load for computations
module purge
module load IMPI/qe-6.5


##############################################
# Declare if you want coordinates from file #
# or from previous relax calculation        #
##############################################


# use "straight" for coordinate from file or "prev" for coordinate from relax
# in both cases you want at least some coordinates
# from "coordinates.txt"
inst=straight


####################################
# Which calculation do you want to #
# perform today?                   #
####################################


# yes or no as y or n
relax=y
scf=n
nscf=n
bands=n
pp_bands=n
pp_dos=n
pp_pdos=n
orbitals=n


##############
```

```
# Files' name #
##############

name="prova"
number_of_processes=2


####################################
# Main variables for calculations #
####################################

prefix=${name}
restart_mode=from_scratch
max_seconds=86390
folder=./SCRATCH_1
celldm1=6.02043457
celldm3=4
num_of_atoms=3
num_of_typ=2
lspinorb=.false.
noncolin=.false.
k_points=1
k_pnt_nscf=21
mixing_beta=0.4
conv_thr=1.0d-8
nbnd=70
degauss=0.0036749309
lsign=.true. # Plot the density with it's signs


###################
# Pseudopotentials #
###################

pseudopot="ATOMIC_SPECIES
Mo     95.94000   Mo.rel-pbe-spn-rrkjus_psl.1.0.0.UPF
S      32.06600   S.rel-pbe-nl-rrkjus_psl.1.0.0.UPF
C      12.01100   C.rel-pbe-n-rrkjus_psl.0.1.UPF"
```

```
##################
# RELAX SUPERCELL #
##################

if [ "$relax" = "y" ] ; then

cat > ./inputs/${name}_relax.in <<EOF
  &CONTROL
    prefix='${prefix}',
    calculation='relax'
    verbosity='high'
    max_seconds=${max_seconds}
    restart_mode='$restart_mode',
    pseudo_dir = '/scratch/corni/alessandro/.pseudopot'
    outdir = '${folder}'
 /
&SYSTEM
    celldm(1) =  $celldm1
    celldm(3) =  $celldm3
    ecutwfc =  62
    ibrav = 4
    nat   = $num_of_atoms
    ntyp  = $num_of_typ
    lspinorb = $lspinorb
    noncolin = $noncolin
/
 &ELECTRONS
    mixing_mode = 'plain'
    mixing_beta = $mixing_beta
    conv_thr =  $conv_thr
 /
 &IONS
   ion_dynamics = "bfgs"
 /
```

```
K_POINTS {automatic}
 $k_points  $k_points  1  0 0 0


$pseudopot


EOF


# Add coordinates from coordinates.txt file in inputs
awk '
/^Begin/{
    found = 1
    next
}
/^End/ {
    found=""
}
found;
' ./inputs/coordinates.txt >> ./inputs/${name}_relax.in


# Run relax calculation
mpirun -np ${number_of_processes} pw.x -inp ./inputs/${name}_relax.in > ./outputs/${name}_1


fi # End of relax


#################
# START WITH SCF #
#################


if [ "$scf" = "y" ] ; then


cat > ./inputs/${name}_scf.in <<EOF
  &CONTROL
    prefix='${prefix}',
    calculation='scf'
    verbosity='high'
```

```
    max_seconds=${max_seconds}

    restart_mode='$restart_mode',

    pseudo_dir = '/scratch/corni/alessandro/.pseudopot'

    outdir = '${folder}'

 /

&SYSTEM

    celldm(1) =  $celldm1

    celldm(3) =  $celldm3

    ecutwfc =  62

    ibrav = 4

    nat   = $num_of_atoms

    ntyp  = $num_of_typ

    nbnd=$nbnd

    lspinorb = $lspinorb

    noncolin = $noncolin

/

 &ELECTRONS

    mixing_mode = 'plain'

    mixing_beta = $mixing_beta

    conv_thr =  $conv_thr

 /


K_POINTS {automatic}

 $k_points  $k_points  1  0 0 0


$pseudopot

EOF


if [ "$inst" = "prev" ]; then


awk '

/^Begin/{

    found = 1

    next

}

/^End/ {
```

```
    found=""
}
found;
' ./outputs/${name}_relax.out >> ./inputs/${name}_scf.in

else

awk '
/^Begin/{
    found = 1
    next
}
/^End/ {
    found=""
}
found;
' ./inputs/coordinates.txt >> ./inputs/${name}_scf.in

fi

# Run SCF calculation
mpirun -np ${number_of_processes} pw.x -inp ./inputs/${name}_scf.in > ./outputs/${name}_scf

# Save the good density in a separate folder
mkdir ./good_dens
cp -rf ${folder} ./good_dens/

fi # End of SCF

####################
# NSCF Calculation #
####################

if [ "$nscf" = "y" ] ; then

cat > ./inputs/${name}_nscf.in <<EOF
```

```
 &CONTROL
    prefix='$prefix',
    calculation='nscf'
    verbosity='high'
    max_seconds=${max_seconds}
    restart_mode='$restart_mode',
    pseudo_dir = '/scratch/corni/alessandro/.pseudopot'
    outdir = '${folder}'
 /
&SYSTEM
    celldm(1) =  $celldm1
    celldm(3) =  $celldm3
    ecutwfc =   62
    ibrav = 4
    nat   = $num_of_atoms
    ntyp  = $num_of_typ
    noncolin = $noncolin
    lspinorb = $lspinorb
    nbnd = $nbnd
/
 &ELECTRONS
    mixing_mode = 'plain'
    mixing_beta = $mixing_beta
    conv_thr =  $conv_thr
 /


K_POINTS {automatic}
 $k_pnt_nscf  $k_pnt_nscf  1  0 0 0


$pseudopot
EOF


if [ "$inst" = "prev" ]; then


awk '
/^Begin/{
```

```
        found = 1
        next
}
/^End/ {
        found=""
}
found;
' ./outputs/${name}_relax.out >> ./inputs/${name}_nscf.in


else


awk '
/^Begin/{
        found = 1
        next
}
/^End/ {
        found=""
}
found;
' ./inputs/coordinates.txt >> ./inputs/${name}_nscf.in


fi


# Run NSCF calculation
mpirun -np ${number_of_processes} pw.x -inp ./inputs/${name}_nscf.in > ./outputs/${name}_ns


fi # End of NSCF


##############################
# Bands structure calculation #
##############################


if [ "$bands" = "y" ] ; then


cat > ./inputs/${name}_bands.in <<EOF
```

```
&CONTROL
    prefix='$prefix',
    calculation='bands'
    verbosity='high'
    max_seconds=${max_seconds}
    restart_mode='$restart_mode',
    pseudo_dir = '/scratch/corni/alessandro/.pseudopot'
    outdir = '${folder}'
 /
&SYSTEM
    celldm(1) =   $celldm1
    celldm(3) =   $celldm3
    ecutwfc =   62
    ibrav = 4
    nat   = $num_of_atoms
    ntyp  = $num_of_typ
    nbnd = $nbnd
    noncolin = $noncolin
    lspinorb = $lspinorb
/
 &ELECTRONS
    mixing_mode = 'plain'
    mixing_beta = $mixing_beta
    conv_thr =  $conv_thr
 /


$pseudopot


K_POINTS {crystal_b}
4
    0.0000000000     0.0000000000     0.0000000000      8 !G
    0.5000000000     0.0000000000     0.0000000000      10 !M
    0.3333333333     0.3333333333     0.0000000000      10 !K
    0.0000000000     0.0000000000     0.0000000000      8 !G
EOF
```

```
if [ "$inst" = "prev" ]; then

awk '
/^Begin/{
    found = 1
    next
}
/^End/ {
    found=""
}
found;
' ./outputs/${name}_relax.out >> ./inputs/${name}_bands.in

else

awk '
/^Begin/{
    found = 1
    next
}
/^End/ {
    found=""
}
found;
' ./inputs/coordinates.txt >> ./inputs/${name}_bands.in

fi

# Run bands structure calculation
mpirun -np ${number_of_processes} pw.x -inp ./inputs/${name}_bands.in > ./outputs/${name}_b

fi # End of BANDS

#######################
# Bands Postprocessing #
#######################
```

```
if [ "$pp_bands" = "y" ] ; then


cat > ./inputs/${name}_bands_pp.in <<EOF
 &BANDS
    prefix = '$prefix'
    outdir = '${folder}/'
    filband = './plots/bands_${name}.dat'
 /
EOF


# Run bands pp
mpirun -np ${number_of_processes} bands.x -inp ./inputs/${name}_bands_pp.in > ./output


fi # End of bands_pp


#####################
# DOS Postprocessing #
#####################


if [ "$pp_dos" = "y" ] ; then


cat > ./inputs/${name}_dos_pp.in <<EOF
&dos
    prefix = '$prefix',
    outdir = '${folder}',
    degauss = $degauss
    fildos = './plots/dos_${name}_Ry${degauss}.dat'
/
eol
EOF


# Run DOS Post-processing
mpirun -np ${number_of_processes} dos.x -inp ./inputs/${name}_dos_pp.in > ./outputs/${
```


```
fi # End of Dos_pp
```

```
#######################
# Proj Dos calculation #
#######################


if [ "$pp_pdos" = "y" ] ; then


cat > ./inputs/${name}_pdos_pp.in <<EOF
&projwfc
    prefix = '$prefix'
    outdir = '${folder}'
    lwrite_overlaps = .true.
    filpdos = './plots/MoS2_pdos.dat'
/
eol
EOF


# Run PDOS Post-processing
mpirun -np ${number_of_processes} projwfc.x -inp ./inputs/${name}_pdos_pp.in > ./outputs/$-


# Sum over all atoms
cd plots/
mkdir sum


sed -i -e 's/E(eV)/E (eV)/g' MoS2*


mpirun -np ${number_of_processes} sumpdos.x *\(Mo\)*\(s*\) > ./sum/atm_Mo_s.dat
mpirun -np ${number_of_processes} sumpdos.x *\(Mo\)*\(p*\) > ./sum/atm_Mo_p.dat
mpirun -np ${number_of_processes} sumpdos.x *\(Mo\)*\(d*\) > ./sum/atm_Mo_d.dat


mpirun -np ${number_of_processes} sumpdos.x *\(S\)*\(s*\) > ./sum/atm_S_s.dat
mpirun -np ${number_of_processes} sumpdos.x *\(S\)*\(p*\) > ./sum/atm_S_p.dat


mpirun -np ${number_of_processes} sumpdos.x *\(C\)*\(s*\) > ./sum/atm_C_s.dat
mpirun -np ${number_of_processes} sumpdos.x *\(C\)*\(p*\) > ./sum/atm_C_p.dat
```

```
cd ..

fi # End of PDos_pp


############
# Orbitals #
############


if [ "$orbitals" = "y" ] ; then


# post-processing for wfns
cat > ./inputs/${name}_orbitals.in << EOF
 &inputpp
    prefix  = '$prefix'
    outdir = '$folder'
    filplot = 'Orb'
    plot_num= 7
    kpoint = 27 ! punto k K
    kband(1) = 25 ! imin
    kband(2) = 28 ! imax
    lsign=$lsign
 /
 &plot
    nfile = 1
    filepp(1) = 'Orb'
    weight(1) = 1.0
    iflag = 3
    output_format = 5
    fileout = 'mos2_other.xsf'
 /
EOF


# Launch post-processing for orbitals
mpirun -np ${number_of_processes} pp.x -inp ./inputs/${name}_orbitals.in > ./outputs/$

fi
```

Bibliography

[1] Sam McArdle, Suguru Endo, Alán Aspuru-Guzik, Simon C Benjamin, and Xiao Yuan. Quantum computational chemistry. *Reviews of Modern Physics*, 92(1):015003, 2020.

[2] Christoph Kloeffel and Daniel Loss. Prospects for spin-based quantum computing in quantum dots. *Annu. Rev. Condens. Matter Phys.*, 4(1):51–81, 2013.

[3] JR Weber, WF Koehl, JB Varley, Anderson Janotti, BB Buckley, CG Van de Walle, and David D Awschalom. Quantum computing with defects. *Proceedings of the National Academy of Sciences*, 107(19):8513–8518, 2010.

[4] John Clarke and Frank K Wilhelm. Superconducting quantum bits. *Nature*, 453(7198):1031–1042, 2008.

[5] Chetan Nayak, Steven H Simon, Ady Stern, Michael Freedman, and Sankar Das Sarma. Non-abelian anyons and topological quantum computation. *Reviews of Modern Physics*, 80(3):1083, 2008.

[6] Mark Saffman, Thad G Walker, and Klaus Mølmer. Quantum information with rydberg atoms. *Reviews of modern physics*, 82(3):2313, 2010.

[7] Bruzewicz, Chiaverini J, McConnell R, and Sage J M. Trapped-ion quantum computing progress and challenges. *Applied Physics Reviews*, 6(3):021314, 2019.

[8] Pieter Kok, William J Munro, Kae Nemoto, Timothy C Ralph, Jonathan P Dowling, and Gerard J Milburn. Linear optical quantum computing with photonic qubits. *Reviews of modern physics*, 79(1):135, 2007.

[9] Songsong Wang, Changliang Han, Liuqi Ye, Guiling Zhang, Yangyang Hu, Weiqi Li, and Yongyuan Jiang. Electronic properties of triangle molybdenum disulfide (mos2) clusters with different sizes and edges. *Molecules*, 26, 2 2021.

[10] Richard Jozsa and Noah Linden. On the role of entanglement in quantum-computational speed-up. *Proceedings of the Royal Society of London. Series A: Mathematical, Physical and Engineering Sciences*, 459(2036):2011–2032, 2003.

[11] David P DiVincenzo. The physical implementation of quantum computation. *Fortschritte der Physik: Progress of Physics*, 48(9-11):771–783, 2000.

[12] Weizhou Cai, Yuwei Ma, Weiting Wang, Chang-Ling Zou, and Luyan Sun. Bosonic quantum error correction codes in superconducting quantum circuits. *Fundamental Research*, 1(1):50–67, 2021.

[13] Wojciech H Zurek et al. Decoherence and the transition from quantum to classical. *Physics today*, 44(10):36–44, 1991.

[14] Jia Chen, Cong Hu, John F Stanton, Stephen Hill, Hai-Ping Cheng, and Xiao-Guang Zhang. Decoherence in molecular electron spin qubits: Insights from quantum many-body simulations. *The Journal of Physical Chemistry Letters*, 11(6):2074–2078, 2020.

[15] David P DiVincenzo. Two-bit gates are universal for quantum computation. *Physical Review A*, 51(2):1015, 1995.

[16] Adriano Barenco, Charles H Bennett, Richard Cleve, David P DiVincenzo, Norman Margolus, Peter Shor, Tycho Sleator, John A Smolin, and Harald Weinfurter. Elementary gates for quantum computation. *Physical review A*, 52(5):3457, 1995.

[17] Dave Bacon, Julia Kempe, Daniel A Lidar, and K Birgitta Whaley. Universal fault-tolerant quantum computation on decoherence-free subspaces. *Physical Review Letters*, 85(8):1758, 2000.

[18] Michael A Nielsen and Isaac Chuang. Quantum computation and quantum information, 2002.

[19] Yasunobu Nakamura, Yu A Pashkin, and JS Tsai. Coherent control of macroscopic quantum states in a single-cooper-pair box. *nature*, 398(6730):786–788, 1999.

[20] Jack D Hidary and Jack D Hidary. *Quantum computing: an applied approach*, volume 1. Springer, 2019.

[21] Marcus D Hughes, Bjoern Lekitsch, Jiddu A Broersma, and Winfried K Hensinger. Microfabricated ion traps. *Contemporary Physics*, 52(6):505–529, 2011.

[22] Hans G Dehmelt. Radiofrequency spectroscopy of stored ions i: Storage. In *Advances in atomic and molecular physics*, volume 3, pages 53–72. Elsevier, 1968.

[23] Trapped ion quantum computers. `https://pennylane.ai/qml/demos/tutorial_trapped_ions.html`.

[24] Colin D Bruzewicz, John Chiaverini, Robert McConnell, and Jeremy M Sage. Trapped-ion quantum computing: Progress and challenges. *Applied Physics Reviews*, 6(2):021314, 2019.

[25] F Schmidt-Kaler, Hartmut Häffner, S Gulde, M Riebe, GPT Lancaster, T Deuschle, C Becher, W Hänsel, J Eschner, Christian F Roos, et al. How to realize a universal quantum gate with trapped ions. *Applied Physics B*, 77:789–796, 2003.

[26] Alejandro Bermudez, Xiaosi Xu, Ramil Nigmatullin, Joe O'Gorman, Vlad Negnevitsky, Philipp Schindler, Thomas Monz, UG Poschinger, Cornelius Hempel, Jonathan Home, et al. Assessing the progress of trapped-ion processors towards fault-tolerant quantum computation. *Physical Review X*, 7(4):041061, 2017.

[27] Adam, Surendra B. Anantharaman, Huiqin Zhang, and Deep Jariwala. Nanomaterials for quantum information science and engineering. *Advanced Materials*, page 2109621, 3 2022.

[28] Steven A Vitale, Daniel Nezich, Joseph O Varghese, Philip Kim, Nuh Gedik, Pablo Jarillo-Herrero, Di Xiao, and Mordechai Rothschild. Valleytronics: opportunities, challenges, and paths forward. *Small*, 14(38):1801483, 2018.

[29] Imran Khan, Brahim Marfoua, and Jisang Hong. Electric field induced giant valley polarization in two dimensional ferromagnetic wse2/crsnse3 heterostructure. *npj 2D Materials and Applications*, 5(1):1–8, 2021.

[30] Tao Hu, Guodong Zhao, Heng Gao, Yabei Wu, Jisang Hong, Alessandro Stroppa, and Wei Ren. Manipulation of valley pseudospin in wse 2/cri 3 heterostructures by the magnetic proximity effect. *Physical Review B*, 101(12):125401, 2020.

[31] Andrea Corna, Léo Bourdet, Romain Maurand, Alessandro Crippa, Dharmraj Kotekar-Patil, Heorhii Bohuslavskyi, Romain Laviéville, Louis Hutin, Sylvain Barraud, Xavier Jehl, et al. Electrically driven electron spin resonance mediated by spin–valley–orbit coupling in a silicon quantum dot. *npj quantum information*, 4(1):6, 2018.

[32] Önder Gül, David J Van Woerkom, Ilse van Weperen, Diana Car, Sébastien R Plissard, Erik PAM Bakkers, and Leo P Kouwenhoven. Towards high mobility insb nanowire devices. *Nanotechnology*, 26(21):215202, 2015.

[33] Henrik A Nilsson, Philippe Caroff, Claes Thelander, Marcus Larsson, Jakob B Wagner, Lars-Erik Wernersson, Lars Samuelson, and HQ Xu. Giant, level-dependent g factors in insb nanowire quantum dots. *Nano letters*, 9(9):3151–3156, 2009.

[34] Selena J Lockyer, Alessandro Chiesa, Grigore A Timco, Eric JL McInnes, Tom S Bennett, Inigo J Vitorica-Yrezebal, Stefano Carretta, and Richard EP Winpenny. Targeting molecular quantum memory with embedded error correction. *Chemical science*, 12(26):9104–9113, 2021.

[35] Marcus W Doherty, Neil B Manson, Paul Delaney, Fedor Jelezko, Jörg Wrachtrup, and Lloyd CL Hollenberg. The nitrogen-vacancy colour centre in diamond. *Physics Reports*, 528(1):1–45, 2013.

[36] Jaewook Lee, Huijin Park, and Hosung Seo. First-principles theory of extending the spin qubit coherence time in hexagonal boron nitride. *arXiv preprint arXiv:2202.04346*, 2022.

[37] Denis D Sukachev, Alp Sipahigil, Christian T Nguyen, Mihir K Bhaskar, Ruffin E Evans, Fedor Jelezko, and Mikhail D Lukin. Silicon-vacancy spin qubit in diamond: a quantum memory exceeding 10 ms with single-shot state readout. *Physical review letters*, 119(22):223602, 2017.

[38] JT Muhonen, JP Dehollain, A Laucht, S Simmons, R Kalra, FE Hudson, AS Dzurak, A Morello, DN Jamieson, JC McCallum, et al. Coherent control via weak measurements in p 31 single-atom electron and nuclear spin qubits. *Physical review B*, 98(15):155201, 2018.

[39] Song Li, Gergő Thiering, Péter Udvarhelyi, Viktor Ivády, and Adam Gali. Carbon defect qubit in two-dimensional ws2. *Nature Communications*, 13(1):1210, 2022.

[40] Paolo Giannozzi, Oscar Baseggio, Pietro Bonfà, Davide Brunato, Roberto Car, Ivan Carnimeo, Carlo Cavazzoni, Stefano De Gironcoli, Pietro Delugas, Fabrizio Ferrari Ruffino, et al. Quantum espresso toward the exascale. *The Journal of chemical physics*, 152(15):154105, 2020.

[41] Attila Szabo and Neil S Ostlund. *Modern quantum chemistry: introduction to advanced electronic structure theory*. Courier Corporation, 2012.

[42] M Marsili, Dott Olivia Pulci, Rodolfo Del Sole, and Piergiorgio Picozza. *Electronic and optical properties of the (111) 2× 1 diamond surface: an ab-initio study*. PhD thesis, Ph. D. thesis. Universitá degli Studi di Roma "Tor Vergata", Rome, 2006.

[43] Pierre Hohenberg and Walter Kohn. Inhomogeneous electron gas. *Physical review*, 136(3B):B864, 1964.

[44] Walter Kohn and Lu Jeu Sham. Self-consistent equations including exchange and correlation effects. *Physical review*, 140(4A):A1133, 1965.

[45] Llewellyn H Thomas. The calculation of atomic fields. In *Mathematical proceedings of the Cambridge philosophical society*, volume 23, pages 542–548. Cambridge University Press, 1927.

[46] Axel D Becke. Density-functional exchange-energy approximation with correct asymptotic behavior. *Physical review A*, 38(6):3098, 1988.

[47] John P Perdew. Density-functional approximation for the correlation energy of the inhomogeneous electron gas. *Physical Review B*, 33(12):8822, 1986.

[48] AD Becke. Density-functional thermochemistry. iii. the role of exact exchange. j. chem. phys., 98: 5648-5652, 1993.

[49] N. W. Ashcroft and N. D. Mermin. *Solid State Physics*. Saunders College Publishing, Orlando, 1976.

[50] GP Francis and MC Payne. Finite basis set corrections to total energy pseudopotential calculations. *Journal of Physics: Condensed Matter*, 2(19):4395, 1990.

[51] Peter Schwerdtfeger. The pseudopotential approximation in electronic structure theory. *ChemPhysChem*, 12(17):3143–3155, 2011.

[52] John P Perdew, Robert G Parr, Mel Levy, and Jose L Balduz Jr. Density-functional theory for fractional particle number: derivative discontinuities of the energy. *Physical Review Letters*, 49(23):1691, 1982.

[53] James F Janak. Proof that $\frac{\partial e}{\partial n_i} = \varepsilon$ in density-functional theory. *Physical Review B*, 18(12):7165, 1978.

[54] Michael Y Toriyama, Alex M Ganose, Maxwell Dylla, Shashwat Anand, Junsoo Park, Madison K Brod, Jason M Munro, Kristin A Persson, Anubhav Jain, and G Jeffrey Snyder. How to analyse a density of states. *Materials Today Electronics*, 1:100002, 2022.

[55] Jolyon Aarons, LG Verga, Nicholas DM Hine, and Chris-Kriton Skylaris. Atom-projected and angular momentum resolved density of states in the onetep code. *Electronic Structure*, 1(3):035002, 2019.

[56] Rafael Roldan, M Pilar López-Sancho, Francisco Guinea, Emmanuele Cappelluti, Jose Angel Silva-Guillén, and Pablo Ordejon. Momentum dependence of spin–orbit interaction effects in single-layer and multi-layer transition metal dichalcogenides. *2D Materials*, 1(3):034003, 2014.

[57] Trapped ion quantum computers. `https://chem.libretexts.org/Bookshelves/Physical_and_Theoretical_Chemistry_Textbook_Maps/Supplemental_Modules_(Physical_and_Theoretical_Chemistry)/Spectroscopy/Electronic_Spectroscopy/Spin-orbit_Coupling`.

[58] Tim Kowalczyk, Shane R Yost, and Troy Van Voorhis. Assessment of the δscf density functional theory approach for electronic excitations in organic dyes. *The Journal of chemical physics*, 134(5):054128, 2011.

[59] Andreas Görling. Density-functional theory beyond the hohenberg-kohn theorem. *Physical Review A*, 59(5):3359, 1999.

[60] Jeppe Gavnholt, Thomas Olsen, Mads Engelund, and Jakob Schiøtz. δself-consistent field method to obtain potential energy surfaces of excited molecules on surfaces. *Physical Review B*, 78(7):075441, 2008.

[61] Irmgard Frank, Jürg Hutter, Dominik Marx, and Michele Parrinello. Molecular dynamics in low-spin excited states. *The Journal of chemical physics*, 108(10):4060–4069, 1998.

[62] Momir Malis, Eva Vandaele, and Sandra Luber. Spin–orbit couplings for nonadiabatic molecular dynamics at the δscf level. *Journal of Chemical Theory and Computation*, 18(7):4082–4094, 2022.

[63] Chris G Van de Walle and Jörg Neugebauer. First-principles calculations for defects and impurities: Applications to iii-nitrides. *Journal of applied physics*, 95(8):3851–3879, 2004.

[64] Christoph Freysoldt and Jörg Neugebauer. First-principles calculations for charged defects at surfaces, interfaces, and two-dimensional materials in the presence of electric fields. *Physical Review B*, 97(20):205425, 2018.

[65] Paolo Giannozzi, Stefano Baroni, Nicola Bonini, Matteo Calandra, Roberto Car, Carlo Cavazzoni, Davide Ceresoli, Guido L Chiarotti, Matteo Cococcioni, Ismaila Dabo, et al. Quantum espresso: a modular and open-source software project for quantum simulations of materials. *Journal of physics: Condensed matter*, 21(39):395502, 2009.

[66] Paolo Giannozzi, Oliviero Andreussi, Thomas Brumme, Oana Bunau, M Buongiorno Nardelli, Matteo Calandra, Roberto Car, Carlo Cavazzoni, Davide Ceresoli, Matteo Cococcioni, et al. Advanced capabilities for materials modelling with quantum espresso. *Journal of physics: Condensed matter*, 29(46):465901, 2017.

[67] Yu Li Huang, Yu Jie Zheng, Zhibo Song, Dongzhi Chi, Andrew TS Wee, and Su Ying Quek. The organic–2d transition metal dichalcogenide heterointerface. *Chemical Society Reviews*, 47(9):3241–3264, 2018.

[68] Tom Ziegler, Arvi Rauk, and Evert J Baerends. On the calculation of multiplet energies by the hartree-fock-slater method. *Theoretica chimica acta*, 43:261–271, 1977.

[69] Francis Dominic Murnaghan. The compressibility of media under extreme pressures. *Proceedings of the National Academy of Sciences*, 30(9):244–247, 1944.

[70] Francis Birch. Finite elastic strain of cubic crystals. *Physical review*, 71(11):809, 1947.

[71] Julia Gusakova, Xingli Wang, Li Lynn Shiau, Anna Krivosheeva, Victor Shaposhnikov, Victor Borisenko, Vasilii Gusakov, and Beng Kang Tay. Electronic properties of bulk and monolayer tmds: theoretical study within dft framework (gvj-2e method). *physica status solidi (a)*, 214(12):1700218, 2017.

[72] Zhiyong Y Zhu, Yingchun C Cheng, and Udo Schwingenschlögl. Giant spin-orbit-induced spin splitting in two-dimensional transition-metal dichalcogenide semiconductors. *Physical Review B*, 84(15):153402, 2011.

[73] Fu Zhang, Yanfu Lu, Daniel S Schulman, Tianyi Zhang, Kazunori Fujisawa, Zhong Lin, Yu Lei, Ana Laura Elias, Saptarshi Das, Susan B Sinnott, et al. Carbon doping of ws2 monolayers: Bandgap reduction and p-type doping transport. *Science advances*, 5(5):eaav5003, 2019.

[74] Ashwin Ramasubramaniam. Large excitonic effects in monolayers of molybdenum and tungsten dichalcogenides. *Physical Review B*, 86(11):115409, 2012.

[75] Shang-Chun Lu and Jean-Pierre Leburton. Electronic structures of defects and magnetic impurities in mos2 monolayers. *Nanoscale research letters*, 9(1):1–9, 2014.

[76] Sunny Gupta, Ji-Hui Yang, and Boris I Yakobson. Two-level quantum systems in two-dimensional materials for single photon emission. *Nano letters*, 19(1):408–414, 2018.

[77] Martti J Puska, S Pöykkö, M Pesola, and Risto M Nieminen. Convergence of supercell calculations for point defects in semiconductors: Vacancy in silicon. *Physical review B*, 58(3):1318, 1998.